

1-2015

Detective quantum efficiency of photon-counting x-ray detectors.

Jesse Tanguay

Seungman Yun

Ho Kyung Kim

Ian A Cunningham

Western University, icunningham@robarts.ca

Follow this and additional works at: <https://ir.lib.uwo.ca/biophysicspub>



Part of the [Medical Biophysics Commons](#)

Citation of this paper:

Tanguay, Jesse; Yun, Seungman; Kim, Ho Kyung; and Cunningham, Ian A, "Detective quantum efficiency of photon-counting x-ray detectors." (2015). *Medical Biophysics Publications*. 14.

<https://ir.lib.uwo.ca/biophysicspub/14>

Detective quantum efficiency of photon-counting x-ray detectors

Jesse Tanguay, Seungman Yun, Ho Kyung Kim, and Ian A. Cunningham

Citation: *Medical Physics* **42**, 491 (2015); doi: 10.1118/1.4903503

View online: <http://dx.doi.org/10.1118/1.4903503>

View Table of Contents: <http://scitation.aip.org/content/aapm/journal/medphys/42/1?ver=pdfcov>

Published by the [American Association of Physicists in Medicine](#)

Articles you may be interested in

[The detective quantum efficiency of photon-counting x-ray detectors using cascaded-systems analyses](#)
Med. Phys. **40**, 041913 (2013); 10.1118/1.4794499

[Cascaded-systems analyses and the detective quantum efficiency of single-Z x-ray detectors including photoelectric, coherent and incoherent interactions](#)
Med. Phys. **40**, 041916 (2013); 10.1118/1.4794495

[Pulse pileup statistics for energy discriminating photon counting x-ray detectors](#)
Med. Phys. **38**, 4265 (2011); 10.1118/1.3592932

[Modeling the performance of a photon counting x-ray detector for CT: Energy response and pulse pileup effects](#)

Med. Phys. **38**, 1089 (2011); 10.1118/1.3539602

[The role of x-ray Swank factor in energy-resolving photon-counting imaging](#)
Med. Phys. **37**, 6205 (2010); 10.1118/1.3512794



 RayStation

**WHAT CAN YOU DO IN
24 SECONDS?**
Watch video >>

ADVANCING
CANCER
TREATMENT

With RayStation, you can optimize and compute clinical dose for a 9-beam IMRT Head and Neck case on a 3 mm dose grid. Also you can use the time, usually spent waiting, to create a new plan or to refine the plan you are working on.

At RaySearch, we want you to feel confident that you have reached the optimal treatment plan for your patient and help you improve treatment quality. This reflects in everything we develop for RayStation.

Don't take our word for granted, watch the demonstration video and book a demo at raysearchlabs.com

RaySearch
Laboratories 

Detective quantum efficiency of photon-counting x-ray detectors

Jesse Tanguay^{a),b)}

*Robarts Research Institute, Western University, London, Ontario N6A 5C1, Canada
and Department of Medical Biophysics, Western University, London, Ontario, N6A 3K7, Canada*

Seungman Yun

*Biomedical Engineering Program, Western University, London, Ontario, N6A 3K7, Canada
and School of Mechanical Engineering, Pusan National University, Jangjeon-dong, Geumjeong-gu,
Busan 609-73, South Korea*

Ho Kyung Kim

*School of Mechanical Engineering, Pusan National University, Jangjeon-dong, Geumjeong-gu,
Busan 609-73, South Korea*

Ian A. Cunningham

*Robarts Research Institute, Western University, London, Ontario N6A 5C1, Canada; Department of Medical
Biophysics, Western University, London, Ontario, N6A 3K7, Canada; and Biomedical Engineering Program,
Western University, London, Ontario, N6A 3K7, Canada*

(Received 5 January 2014; revised 3 November 2014; accepted for publication 18 November 2014;
published 5 January 2015)

Purpose: Single-photon-counting (SPC) x-ray imaging has the potential to improve image quality and enable novel energy-dependent imaging methods. Similar to conventional detectors, optimizing image SPC quality will require systems that produce the highest possible detective quantum efficiency (DQE). This paper builds on the cascaded-systems analysis (CSA) framework to develop a comprehensive description of the DQE of SPC detectors that implement adaptive binning.

Methods: The DQE of SPC systems can be described using the CSA approach by propagating the probability density function (PDF) of the number of image-forming quanta through simple quantum processes. New relationships are developed to describe PDF transfer through serial and parallel cascades to accommodate scatter reabsorption. Results are applied to hypothetical silicon and selenium-based flat-panel SPC detectors including the effects of reabsorption of characteristic/scatter photons from photoelectric and Compton interactions, stochastic conversion of x-ray energy to secondary quanta, depth-dependent charge collection, and electronic noise. Results are compared with a Monte Carlo study.

Results: Depth-dependent collection efficiency can result in substantial broadening of photopeaks that in turn may result in reduced DQE at lower x-ray energies (20–45 keV). Double-counting interaction events caused by reabsorption of characteristic/scatter photons may result in falsely inflated image signal-to-noise ratio and potential overestimation of the DQE.

Conclusions: The CSA approach is extended to describe signal and noise propagation through photoelectric and Compton interactions in SPC detectors, including the effects of escape and reabsorption of emission/scatter photons. High-performance SPC systems can be achieved but only for certain combinations of secondary conversion gain, depth-dependent collection efficiency, electronic noise, and reabsorption characteristics. © 2015 American Association of Physicists in Medicine. [<http://dx.doi.org/10.1118/1.4903503>]

Key words: photon counting, x-ray imaging, cascaded systems analysis, spectral imaging, detective quantum efficiency

1. INTRODUCTION

Advances in x-ray detector technology have enabled single-photon-counting (SPC) x-ray detectors with the ability to identify individual photon interactions. When equipped with multithresholding circuits, these systems enable energy-resolving photon-counting (EPC) imaging where the deposited energy from each interacting x-ray photon is estimated.^{1–7} It is anticipated that the resulting spectral distribution of energy-depositing events will lead to advanced spectroscopic procedures^{8–14} and improve image quality by reducing image

noise from random physical processes including Swank and electronic readout noise.^{7,15}

While photon-counting methods are receiving a great deal of interest, there remain many challenges to overcome. State-of-the-art systems are capable of count rates that may be adequate for some applications including mammography^{16–20} and breast computed tomography,^{21–24} but remain restrictive.^{25,26} In addition, charge sharing between neighboring detector elements can cause a degradation of image quality^{27,28} and loss of spectral information.^{4,27–30} This effect is mitigated with techniques that sum charges in neighboring

elements surrounding an interaction and assigns them to a single element, such as that implemented in the MEDIPIX3 prototype.⁴ In the MEDIPIX approach, elements are clustered into larger binned elements, the total charge generated in binned elements is determined, and a count is attributed to the element (within each cluster) with the largest signal. We call these methods “adaptive binning” and some form of adaptive binning will almost certainly be required to achieve high-quality images.

It is also true that these systems will produce the best possible images when they are optimized to achieve the best possible detective quantum efficiency (DQE).³¹ Cascaded-systems analysis^{32–41} (CSA) has been successful in the development of theoretical models of the DQE, important in the development of conventional energy-integrating systems, and was recently extended to describe the zero-frequency DQE of SPC detectors that implement adaptive binning.^{42,43} In particular, it was shown that $DQE(0)$ can be expressed in terms of the mean photon-counting signal and associated Wiener noise power spectrum (NPS) and that both can be obtained from the probability density function (PDF) of detector signals. For SPC systems, this leads to⁴³

$$DQE(0) = \alpha I_{\text{SPC}}, \quad (1)$$

where α represents the detector quantum efficiency and I_{SPC} is a noise factor ($I_{\text{SPC}} \leq 1$) equal to the probability that a true photon count is recorded given an interaction event (true-positive fraction). This latter term has a pleasing symmetry with the Swank-noise factor^{38,44–46} for conventional energy-integrating systems with I_{SPC} becoming the “SPC Swank factor” accounting for degradation in image signal-to-noise ratio (SNR) due to stochastic energy deposition, conversion, and charge-collection processes. Equation (1) is a good description of SPC detector performance when there is minimal noise aliasing at zero spatial frequency, effective adaptive binning approaches are implemented, and a threshold is chosen such that false counts due to electronic noise are suppressed.

Tanguay *et al.*⁴³ described a method of determining I_{SPC} from the PDF of the total number of detected secondary quanta per x-ray interaction and showed this PDF can be determined by propagating the PDF of the number of image-forming quanta at each stage through a serial cascade of quantum processes. While this established the importance and utility of the cascaded-systems approach for describing the DQE of SPC systems, it was restricted to the simplistic case where all photon energy is deposited at the primary-interaction site, ignoring photoelectric and Compton emission/scatter photons that escape the detector or are reabsorbed at a remote-interaction site. In the case of reabsorption, photon energy is converted to secondary quanta at both primary-interaction and reabsorption sites, resulting in a complicated energy response function.⁴⁷ In addition, liberation of secondary quanta (e.g., charges in a photoconductor or optical photons in a scintillator) is a stochastic process and the PDF when energy is deposited at one site differs to that when the same energy is deposited at multiple sites.

The purpose of this paper is to extend the cascaded-systems approach to describe the zero-frequency DQE of SPC systems

including the effects of x-ray reabsorption, imperfect charge collection, and additive readout noise. This is accomplished by describing PDF transfer through parallel cascades of quantum processes and developing a relatively simple closed-form expression for the PDF under conditions of importance for SPC imaging. The utility of this approach is demonstrated in an analysis of the zero-frequency DQE of hypothetical silicon- and selenium-based flat-panel SPC detectors.

2. THEORY

2.A. I_{SPC} and energy-response function R

The SPC noise factor I_{SPC} is equal to the true-positive fraction of counting interaction events.^{42,43} The detector signal \tilde{d} after adaptive binning and prior to thresholding is equivalent to the signal from a large detector element in which the x-ray photon always interacts near the center and readout noise is equal to the quadrature sum of noise from each element in the binned cluster. For an interacting photon of energy E , \tilde{d} is used to estimate deposited photon energy $\tilde{\varepsilon}$ where, for a linear x-ray detector, $\tilde{\varepsilon} = \kappa \tilde{d}$ for some constant κ . It is convenient to characterize the system response in terms of the energy response function $R(\varepsilon, E)$ which is equal to the probability density of $\tilde{\varepsilon}$ given interacting energy E . Letting $p_d(d|E)$ represent the PDF of \tilde{d} given an interaction yields

$$R(\varepsilon, E) = \frac{1}{\kappa} p_d(d|E)|_{d=\varepsilon/\kappa} \quad (2)$$

and the SPC noise factor is then given by⁴³

$$I_{\text{SPC}} = \int_{\kappa t}^{\infty} R(\varepsilon, E) d\varepsilon = \int_t^{\infty} p_d(d|E) dd, \quad (3)$$

where t is a threshold used to separate x-ray interaction events from electronic noise. This result shows that I_{SPC} can be determined from a knowledge of the PDF of (binned) detector signals. Multiple thresholds can be used to determine the spectral distribution of $\tilde{\varepsilon}$.

2.B. Mean number of photon counts

The number of counts reported by a SPC system is given by the RV \tilde{c} . For fast readouts and detectors that implement adaptive binning to sum charges in neighboring elements surrounding an interaction and assign them to a single element, the mean \bar{c} is given by⁴³

$$\bar{c} = \bar{q}_0 \alpha I_{\text{SPC}} \left[1 + \frac{\zeta}{\lambda \alpha I_{\text{SPC}}} \right], \quad (4)$$

where \bar{q}_0 [mm⁻²] describes the mean number of incident quanta, $\lambda = \bar{q}_0 a_t \alpha$ ($\lambda \ll 1$) describes the number incident during integration time a_t , I_{SPC} is given by Eq. (3), and ζ represents the probability of observing a false count due to electronic readout noise. Unlike conventional energy-integrating detectors, it is seen readout noise may result in an increase in the mean SPC image signal. Suppression of false noise counts requires a threshold high enough to keep the false-positive fraction low and the second term in square brackets small.

2.C. Determining R from the PDF of image quanta

Equations (3) and (4) show that I_{SPC} and \bar{c} are determined by the energy response function R and in turn by the PDF of \tilde{d} . Yun et al.⁴⁷ described R for selected x-ray convertor materials, including the effects of random x-ray energy-depositing processes, for deterministic conversion of x-ray energy to secondary quanta with negligible pulse pileup.^{48–50} Here, we describe a method of obtaining R from the PDF of \tilde{d} that includes the effects of x-ray reabsorption and stochastic conversion and collection processes. We start by summarizing simpler PDF-transfer relationships and then extend to include a description of x-ray reabsorption.

2.C.1. Elementary processes

We refer to five simple processes that are used frequently as “elementary” processes, consisting of (1) quantum gain, (2) quantum selection, (3) quantum scatter, (4) general gain, (5) general filter, and (6) sampling. Quantum gain^{32,33} is the process of replacing the j th point in a distribution of points with \tilde{g}_j (a random variable with integer-only sample values) points at the same location, such as liberation of secondary quanta (optical photons or e–h pairs). Quantum selection³³ is a special case where a random selection of input points is passed to the output (quantum gain by factor 1 or 0), such as the selection of interacting quanta from a distribution of incident quanta. Quantum scatter^{32,33} is the random relocation of individual points in the image plane according to a specified PDF, such as charge carrier diffusion in a semiconductor. General gain is the scaling of an input signal by a gain RV that may have a continuum of values (e.g., amplifier gain) and general filter corresponds to any deterministic image-blurring process that can be described as a convolution operation.³⁴ Sampling describes the process of evaluating the detector signal at discrete locations corresponding to the center of detector elements and can be represented by multiplication with a series of Dirac delta functions.⁵¹ Temporal lag effects can be incorporated⁵² and these processes combined in serial and parallel cascades^{53,54} to create comprehensive models of signal and noise (and thereby DQE) of complex quantum-based imaging systems.

2.C.2. PDF following a cascade of elementary processes

Letting \tilde{N}_i represent the total number of image quanta (points) after the i th stage in a serial cascade of quantum processes gives the PDF of \tilde{N}_i as⁴³

$$p_{N_i}(N_i) = \int p_{N_i}(N_i|N_{i-1})p_{N_{i-1}}(N_{i-1})dN_{i-1}, \tag{5}$$

where $p_{N_i}(N_i|N_{i-1})$ represents the conditional PDF of \tilde{N}_i given \tilde{N}_{i-1} . Recursive application yields the PDF after n processes

$$p_{N_n}(N_n) = \int p_{N_n}(N_n|N_{n-1}) \int p_{N_{n-1}}(N_{n-1}|N_{n-2}) \dots \int p_{N_1}(N_1|N_0)p_{N_0}(N_0)dN_0 \dots dN_{n-1}, \tag{6}$$

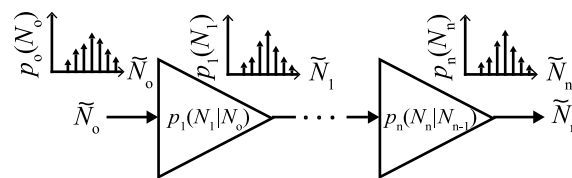


Fig. 1. Schematic representation of PDF transfer in quantum processes. Each PDF consists of scaled Dirac δ -functions describing probabilities of integer numbers of quanta.

where $p_{N_0}(N_0)$ is the PDF of the number of incident (x-ray) quanta, as illustrated in Fig. 1, with each process characterized by a conditional PDF. Since the number of quanta must be an integer, both $p_{N_i}(N_i)$ and $p_{N_i}(N_i|N_{i-1})$ are generalized functions consisting of a sequence of scaled δ -functions at integer values of N .

Gain stages are characterized by an integer gain RV \tilde{g} having PDF p_g and the total number of quanta in the output comes from replacing each quantum in the input with \tilde{g} quanta. Since p_g is assumed identical for input quanta having the same energy, for monoenergetic photon fluence, the conditional PDF is expressed as p_g convolved with itself $N_{i-1} - 1$ times,^{43,55}

$$p_{N_i}(N_i|N_{i-1}) = (p_g *^{N_{i-1}-1} p_g)(N_{i-1}) \tag{7}$$

expressed as a function of N_{i-1} , where

$$p_g(g) = \sum_k \text{pr}_g(k) \delta(g - k) \tag{8}$$

and pr_g represents the probability mass function (PMF) of \tilde{g} with the summation over all possible values of \tilde{g} . Extension to polyenergetic fluence would require additional averaging over the incident photon spectrum. For quantum scatter, the number of quanta is unchanged and the conditional PDF is a unity operator.

Three special cases of quantum gain are illustrated. For each, pr_g must be normalized over the domain of integer values.

2.C.2.a. *Poisson gain.* For Poisson gain with mean \bar{g} ,

$$\text{pr}_g(k) = \frac{\bar{g}^k e^{-\bar{g}}}{k!} \tag{9}$$

for integer k . Combining with Eqs. (7) and (8) yields a Poisson distribution with mean $\bar{g}N_{i-1}$,^{42,55}

$$p_{N_i}(N_i|N_{i-1}) = \sum_j \frac{\bar{g}^j N_{i-1}^j e^{-\bar{g}N_{i-1}}}{j!} \delta(N_i - j). \tag{10}$$

2.C.2.b. *Deterministic gain.* For the case of deterministic gain,

$$\text{pr}_g(k) = \delta_{k\bar{g}}, \tag{11}$$

where $\delta_{k\bar{g}}$ represents the Kronecker delta and is equal to 1 when $k = \bar{g}$ and 0 otherwise. The translation property of the Dirac δ -function yields

$$p_{N_i}(N_i|N_{i-1}) = \delta(N_i - \bar{g}N_{i-1}). \tag{12}$$

2.C.2.c. *Selection.* Quantum selection is a special case of quantum gain where \tilde{g} is a Bernoulli RV assuming values of

1 or 0 only with probabilities α and $1 - \alpha$, respectively, and pr_g is given by a Bernoulli distribution

$$\text{pr}_g(k) = \alpha^k(1 - \alpha)^{1-k}, \tag{13}$$

resulting in a Binomial distribution^{42,55}

$$p_{N_i}(N_i|N_{i-1}) = \sum_j \binom{N_{i-1}}{j} \alpha^j(1 - \alpha)^{N_{i-1}-j} \delta(N_i - j). \tag{14}$$

These results and others, summarized in Appendix B, may be used in combination with Eq. (6) to provide a complete description of the PDF for a single serial cascade of energy-depositing events. This result is generalized to include scatter-reabsorption events using a parallel-cascades approach in Sec. 2.C.3. A list of selected variables is included in Appendix A.

2.C.3. PDF following parallel cascades

For the case of multiple energy-depositing paths (Fig. 2), such as energy deposition at primary-interaction and scatter-reabsorption sites, the total number of secondary quanta is the sum from all paths.⁵³ For the case of two paths, the PDF of the sum $\tilde{N}_{A+B} = \tilde{N}_A + \tilde{N}_B$ is given by⁵⁵

$$p_{N_{A+B}}(N_{A+B}) = \int_{-\infty}^{+\infty} p_{N_{A,B}}(N_{A+B} - N_B, N_B) dN_B, \tag{15}$$

where $p_{N_{A,B}}$ is the joint PDF describing the probability of observing \tilde{N}_A and \tilde{N}_B quanta from paths A and B, respectively. When \tilde{N}_A and \tilde{N}_B are independent RVs, $p_{N_{A,B}} = p_{N_A} p_{N_B}$, giving

$$p_{N_{A+B}}(N_{A+B}) = p_{N_A}(N_{A+B}) * p_{N_B}(N_{A+B}). \tag{16}$$

Equations (15) and (16) give the PDF of a sum of quanta from correlated and uncorrelated paths, respectively.

Of particular importance in this application is when the input to each path is a subset of a common input distribution as illustrated in Fig. 2. The process of selecting quanta for each path is a branching process in the cascade model.

2.C.3.a. Joint PDF and branch points. The branching process represents a sequence of trials where the j th trial is a random selection of the j th point to follow paths A and/or B with probabilities $\tilde{\xi}_A$ and $\tilde{\xi}_B$, respectively.⁵³ This

could represent selection of incident photons that undergo photoelectric or Compton interactions. Each trial is described by Bernoulli RVs $\tilde{\xi}_{j,A}$ and $\tilde{\xi}_{j,B}$ having sample values 1 or 0 corresponding to being selected, or not, for each path. Each trial is independent but correlations may exist between $\tilde{\xi}_{j,A}$ and $\tilde{\xi}_{j,B}$ as described by the joint PDF⁵⁵

$$p_{\xi_{j,A}, \xi_{j,B}}(\xi_{j,A}, \xi_{j,B}) = \sum_{k=0}^1 \sum_{l=0}^1 P(\xi_{j,A} = k \text{ and } \xi_{j,B} = l) \times \delta(\xi_{j,A} - k) \delta(\xi_{j,B} - l), \tag{17}$$

where $P(\xi_{j,A} = k \text{ and } \xi_{j,B} = l)$ gives the probability that $\tilde{\xi}_{j,A} = k$ and $\tilde{\xi}_{j,B} = l$. We use Eq. (17) to derive an expression for $p_{N_{A+B}}(N_{A+B})$ in Eq. (15) by first considering the simpler case of one input quantum to the branch point and then generalize to a random number.

One input quantum, $N_0 = 1$. This case represents the situation of a single photon interaction in an adaptively binned element during one integration period, where there can be only one ($\tilde{\xi}_{1,A} = 1$) or zero ($\tilde{\xi}_{1,A} = 0$) quanta following path A in Fig. 2, and similarly for path B,

$$\tilde{N}_A = \tilde{\xi}_{1,A}, \quad \tilde{N}_B = \tilde{\xi}_{1,B}. \tag{18}$$

Therefore,

$$p_{N_{A,B}}(N_A, N_B | N_0 = 1) = p_{\xi_{1,A}, \xi_{1,B}}(N_A, N_B), \tag{19}$$

where $p_{\xi_{j,A}, \xi_{j,B}}(N_A, N_B)$ represents the joint PDF of $\tilde{\xi}_{1,A}$ and $\tilde{\xi}_{1,B}$ evaluated at N_A and N_B .

Random number of input quanta, \tilde{N}_0 . A more general case is to accommodate a random number of quanta interacting in an adaptively binned element during a single integration period, including multiple counts, giving

$$\tilde{N}_A = \sum_{j=1}^{\tilde{N}_0} \tilde{\xi}_{j,A}, \quad \tilde{N}_B = \sum_{j=1}^{\tilde{N}_0} \tilde{\xi}_{j,B}. \tag{20}$$

Assuming the joint PDF for $\tilde{\xi}_{j,A}$ and $\tilde{\xi}_{j,B}$ is the same for all j , \tilde{N}_A and \tilde{N}_B are sums of \tilde{N}_0 identically distributed independent RVs. We show in Appendix C that $p_{N_{A,B}}$ given \tilde{N}_0 input quanta is then given by

$$p_{N_{A,B}}(N_A, N_B | \tilde{N}_0) = (p_{\xi_A, \xi_B} * \tilde{N}_0^{-1} p_{\xi_A, \xi_B})(N_A, N_B), \tag{21}$$

where the right-hand side denotes the 2D convolution of $p_{\xi_A, \xi_B}(\xi_A, \xi_B)$ with itself $\tilde{N}_0 - 1$ times. Averaging over \tilde{N}_0 yields

$$p_{N_{A,B}}(N_A, N_B) = \int (p_{\xi_A, \xi_B} * \tilde{N}_0^{-1} p_{\xi_A, \xi_B})(N_A, N_B) p_{N_0}(N_0) dN_0, \tag{22}$$

showing that the joint PDF of the number of quanta in two random subsets of a common input distribution is fully described by the joint PDF of selection variables $\tilde{\xi}_{j,A}$ and $\tilde{\xi}_{j,B}$, and the PDF of \tilde{N}_0 .

2.C.3.b. Joint PDF following cascades of elementary processes. A more general case involves the joint statistics of the number of quanta in two paths after undergoing serial cascades of elementary processes as illustrated in Fig. 3. The RVs $\tilde{N}_{A,i}$ and $\tilde{N}_{B,i}$ represent the number of quanta after the i th

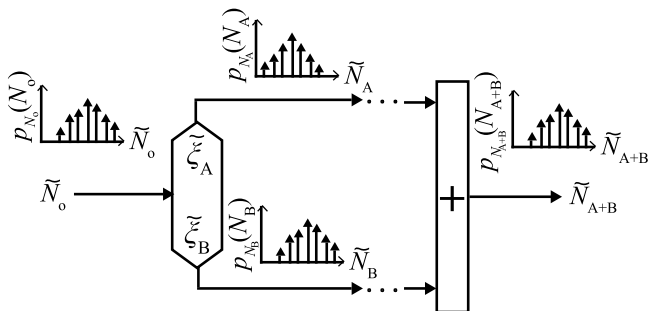


FIG. 2. Illustration of PDF transfer where \tilde{N}_0 is separated into parallel cascades A and B and then recombined.

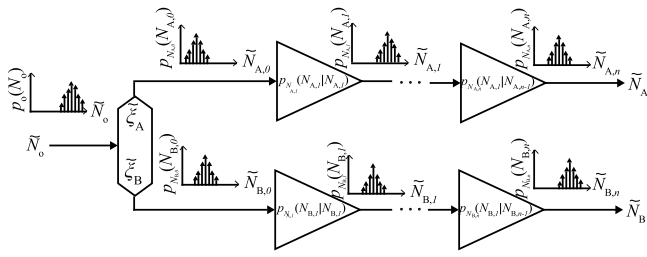


FIG. 3. Illustration of PDF transfer through parallel cascades of elementary quantum processes.

elementary process of each path. Similar to Sec. 2.C.3.a, we derive an expression for $p_{N_{A,B}}$ by first considering the simple case of one input quantum.

One input quantum, $N_0 = 1$. In the parallel cascades of elementary processes in Fig. 3, $\tilde{N}_{A,i} = \tilde{N}_{j,A,i}$ represents the number of secondary quanta for the j th input quantum after the i th process of path A (and similarly for path B). For one input quantum, we have

$$\tilde{N}_A = \tilde{N}_{1,A,n_A}, \quad \tilde{N}_B = \tilde{N}_{1,B,n_B}, \quad (23)$$

where n_A identifies the last process in path A, and similarly for path B. Assuming processes in path A is independent of those in path B yields

$$p_{N_{A,B}}(N_A, N_B | \tilde{\xi}_{1,A}, \tilde{\xi}_{1,B}, N_0 = 1) = p_{N_{1,A}}(N_{1,A} | \tilde{\xi}_{1,A}) p_{N_{1,B}}(N_{1,B} | \tilde{\xi}_{1,B}), \quad (24)$$

where $p_{N_{1,A}}(N_{1,A} | \tilde{\xi}_{1,A})$ represents the PDF of \tilde{N}_{1,A,n_A} given $\tilde{\xi}_{1,A}$, and similarly for path B, where we have dropped explicit dependence on n_A and n_B . Averaging over $\tilde{\xi}_{1,A}$ and $\tilde{\xi}_{1,B}$ yields

$$p_{N_{A,B}}(N_A, N_B | N_0 = 1) = \langle p \rangle_{\xi_A, \xi_B}, \quad (25)$$

where $\langle \rangle_{\xi_A, \xi_B}$ represents averaging over $\tilde{\xi}_{j,A}$ and $\tilde{\xi}_{j,B}$, and

$$\begin{aligned} \langle p \rangle_{\xi_A, \xi_B} &= \langle p_{N_A}(N_A | \xi_A) p_{N_B}(N_B | \xi_B) \rangle_{\xi_A, \xi_B} \\ &= \iint p_{N_A}(N_A | \xi_A) p_{N_B}(N_B | \xi_B) \\ &\quad \times p_{\xi_A, \xi_B}(\xi_A, \xi_B) d\xi_A d\xi_B, \end{aligned} \quad (26)$$

where $p_{N_A}(N_A | \xi_A)$ represents the PDF of \tilde{N}_A given $\tilde{\xi}_{j,A}$ for one trial and is obtained from Eq. (6)

$$\begin{aligned} p_{N_A}(N_A | \xi_A) &= \int p_{N_{A,n}}(N_{A,n} | N_{A,n-1}) \\ &\quad \times \int p_{N_{A,n-1}}(N_{A,n-1} | N_{A,n-2}) \\ &\quad \dots \int p_{N_{A,0}}(N_{A,0} | \xi_A) dN_{A,0} \dots dN_{A,n-1} \end{aligned} \quad (27)$$

and similarly for $p_{N_B}(N_B | \xi_B)$.

Random number of input quanta, \tilde{N}_0 . Similar to Eq. (20), the numbers of quanta from paths A and B are

$$\tilde{N}_A = \sum_{j=1}^{\tilde{N}_0} \tilde{N}_{j,A,n_A}, \quad \tilde{N}_B = \sum_{j=1}^{\tilde{N}_0} \tilde{N}_{j,B,n_B}. \quad (28)$$

In Appendix C, we show that because each process in path A is independent of those in B and $\tilde{\xi}_{j,A}$ is independent of $\tilde{\xi}_{i,A}$

for $i \neq j$ (and similarly for $\tilde{\xi}_{j,B}$), the joint PDF of \tilde{N}_A and \tilde{N}_B given \tilde{N}_0 is

$$p_{N_{A,B}}(N_A, N_B | \tilde{N}_0) = \langle p \rangle_{\xi_A, \xi_B} * \tilde{N}_0^{-1} \langle p \rangle_{\xi_A, \xi_B}, \quad (29)$$

where $\langle p \rangle_{\xi_A, \xi_B}$ is the joint PDF given one input quantum in Eq. (25). Averaging over all possible values of \tilde{N}_0 yields

$$p_{N_{A,B}}(N_A, N_B) = \int [\langle p \rangle_{\xi_A, \xi_B} * \tilde{N}_0^{-1} \langle p \rangle_{\xi_A, \xi_B}] p_{N_0}(N_0) dN_0. \quad (30)$$

This is a general PDF-transfer relationship between $p_{N_{A,B}}$ and p_{N_0} and shows that the joint statistics of \tilde{N}_A and \tilde{N}_B are determined by the joint statistics of $\tilde{\xi}_A$ and $\tilde{\xi}_B$, the elementary processes in paths A and B, and the input PDF p_{N_0} .

We further consider two important branch points: (i) each input quantum is selected for *either* path A or B (Bernoulli branch), and (ii) each input quantum is selected for *both* paths A and B (cascade fork).⁵³

2.C.3.c. Bernoulli branch. A Bernoulli branch may, for example, describe separation of photoelectric interactions that produce a characteristic emission from those that do not.^{37,38,41,53} The joint PDF of $\tilde{\xi}_{j,A}$ and $\tilde{\xi}_{j,B}$ is

$$p_{\xi_A, \xi_B}(\xi_A, \xi_B) = \bar{\xi}_A \delta(\xi_A - 1) \delta(\xi_B) + \bar{\xi}_B \delta(\xi_A) \delta(\xi_B - 1) \quad (31)$$

from Eq. (17). Combining this with Eq. (25) yields

$$\begin{aligned} \langle p \rangle_{\xi_A, \xi_B} &= \bar{\xi}_A p_{N_A}(N_A | \xi_A = 1) p_{N_B}(N_B | \xi_B = 0) \\ &\quad + \bar{\xi}_B p_{N_A}(N_A | \xi_A = 0) p_{N_B}(N_B | \xi_B = 1), \end{aligned} \quad (32)$$

where $p_{N_A}(N_A | \xi_A = 0) = \delta(N_A)$ and $p_{N_B}(N_B | \xi_B = 0) = \delta(N_B)$. Combining the above expression with Eq. (30) yields $p_{N_{A,B}}$ after multiple elementary processes.

One input quantum, $N_0 = 1$. Combining Eqs. (15) and (32) yields

$$\begin{aligned} p_{N_{A+B}}(N_{A+B} | N_0 = 1) &= \bar{\xi}_A p_{N_A}(N_{A+B} | \xi_A = 1) \\ &\quad + \bar{\xi}_B p_{N_B}(N_{A+B} | \xi_B = 1). \end{aligned} \quad (33)$$

This describes the expected result that when an input quantum is selected for only one path, the PDF of the total number of output quanta is equal to the weighted combination of each.

2.C.3.d. Cascade fork. A cascade fork may, for example, describe the situation where a photon that has interacted through the Compton effect deposits energy at the site of primary interaction and at a remote site following reabsorption of a Compton-scatter photon. The joint PDF of selection variables is then given by

$$p_{\xi_A, \xi_B}(\xi_A, \xi_B) = \delta(\xi_A - 1) \delta(\xi_B - 1) \quad (34)$$

and therefore

$$\langle p \rangle_{\xi_A, \xi_B} = p_{N_A}(N_A | \xi_A = 1) p_{N_B}(N_B | \xi_B = 1). \quad (35)$$

Combining the above expression with Eq. (30) yields $p_{N_{A,B}}$ after multiple elementary processes.

One input quantum, $N_0 = 1$. Combining Eqs. (15) and (35) yields

$$\begin{aligned} p_{N_{A+B}}(N_{A+B} | N_0 = 1) &= p_{N_A}(N_{A+B} | \xi_A = 1) * p_{N_B}(N_{A+B} | \xi_B = 1). \end{aligned} \quad (36)$$

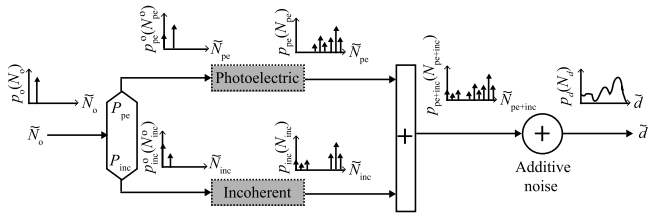


FIG. 4. Schematic illustration of the parallel CSA model describing PDF transfer of the total number of secondary quanta through photoelectric interactions, incoherent interactions, and additive electronic noise using parallel cascades. The RV \tilde{N}_0 is the total number of incident x-ray quanta in one readout and is set to unity.

Equations (33) and (36) are important results of this work. They are special cases of a branch point where the signal from an interacting photon passes through either only one [Eq. (33)] or both [Eq. (36)] of two paths and allow us to use the complex models of Figs. 4 and 5 to describe PDF transfer through photoelectric and Compton interactions. In Sec. 2.D, we use these results to determine the energy response function and in turn the zero-frequency DQE of hypothetical selenium-based and silicon-based SPC detectors.

2.D. Liberation of secondary quanta in x-ray convertor

Figure 4 illustrates the parallel-cascade model we use to describe energy deposition in an x-ray convertor including the effects of stochastic energy deposition through photoelectric or incoherent scattering, conversion to secondary quanta, and collection of secondary quanta, similar to that described by Yun *et al.*⁴¹ Figure 4 does not illustrate subsequent thresholding and sampling stages discussed in detail by Tanguay *et al.*⁴³ In all cases, we assume flat-panel SPC systems. Our goal is to describe the PDF of the total number of secondary quanta \tilde{N}_{tot} collected by detector elements per interacting x-ray photon. We therefore let $p_{N_0}(N_0) = \delta(N_0 - 1)$ and assume large adaptively binned pixels such that the probability of reabsorption of characteristic or Compton-scatter x-rays in neighboring elements is negligible. This may be a good approximation for systems that use adaptive binning to sum signals from neighboring pixels to get the total energy deposited for every interacting x-ray photon.

The output from each path is the total number of quanta collected from either photoelectric or incoherent interactions. From Eq. (15), the total number of collected secondaries $\tilde{N}_{\text{tot}} = \tilde{N}_{\text{pe}} + \tilde{N}_{\text{inc}}$ is given by

$$p_{N_{\text{tot}}}(N_{\text{tot}}) = \int_{-\infty}^{+\infty} p_{N_{\text{pe,inc}}}(N_{\text{tot}} - N_{\text{pe}}, N_{\text{pe}}) dN_{\text{pe}}, \quad (37)$$

where $p_{N_{\text{pe,inc}}}(N_{\text{pe}}, N_{\text{inc}})$ is the joint PDF of \tilde{N}_{pe} and \tilde{N}_{inc} . The Bernoulli branch in Fig. 4 and Eq. (32) gives

$$p_{N_{\text{tot}}}(N_{\text{tot}}) = \bar{\xi}_{\text{pe}} p_{N_{\text{pe}}}(N_{\text{tot}} | \xi_{\text{pe}} = 1) + \bar{\xi}_{\text{inc}} p_{N_{\text{inc}}}(N_{\text{tot}} | \xi_{\text{inc}} = 1), \quad (38)$$

where $\bar{\xi}_{\text{pe}}$ and $\bar{\xi}_{\text{inc}}$ represent the relative probabilities of photoelectric absorption and incoherent scattering.^{41,47}

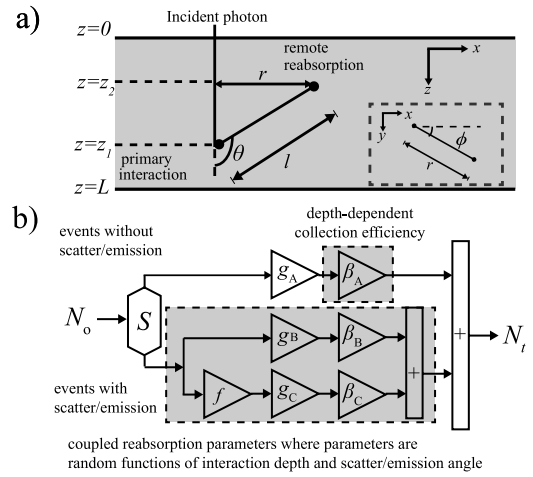


FIG. 5. Schematic illustration of the generalized interaction model. (a) Incident x-ray photon interacts in x-ray convertor at depth z_1 with subsequent production of a scatter photon at polar angle θ and azimuthal angle ϕ . (b) CSA model describing events that liberate secondary quanta from (path A) primary-interaction site when no scatter/emission photon is generated; (path B) primary-interaction site when a scatter/emission photon is generated; and (path C) remote reabsorption of scatter/emission photon.

Equation (38) shows that a description of $p_{N_{\text{tot}}}(N_{\text{tot}})$ requires the PDFs of the number of collected secondaries resulting from photoelectric and incoherent interactions. These processes are similar in that each may result in emission and reabsorption of a fluorescent/scatter photon. It is therefore convenient to describe photoelectric and incoherent interactions as two special cases of a “generalized” interaction process.

2.E. Generalized x-ray interaction process

Each shaded box in Fig. 4 is a special case of the generalized interaction process in Fig. 5. When used, subscript t represents the interaction type, photoelectric (pe) or incoherent (inc). As illustrated, an incident photon interacts at depth \tilde{z}_1 in the x-ray convertor material and may generate a scatter photon with probability S at scatter angle $\tilde{\theta}$ and azimuthal angle $\tilde{\phi}$ that may be reabsorbed at depth \tilde{z}_2 with probability f . Secondary quanta (electron–hole pairs in a photoconductor) are liberated at both primary-interaction and reabsorption sites unless the scatter photon escapes the detector. This model is based on that described by Yun *et al.*⁴¹ with the extension to depth-dependent collection efficiency.

The collection efficiencies β for each path in Fig. 5 are functions of interaction depths \tilde{z}_1 and \tilde{z}_2 , which are themselves RVs. The concept of using gain and/or selection variables that are functions of random variables was introduced by Van Metter and Rabbani⁵⁶ who called these input-labeled random processes. We adopt this idea to describe the depth-dependent collection efficiency in the top shaded path of Fig. 5(b). However, in the lower shaded box, *all* processes are functions of \tilde{z}_1 and/or $\tilde{\theta}$. In addition, these processes are coupled because they are dependent on the same \tilde{z}_1 and $\tilde{\theta}$ sample values for each interacting photon. In Appendix C we generalize the previous derivation of the PDF of the total

number of image quanta from parallel cascades to include these input-labeled parallel processes. The result is used to calculate the PDF of the number of quanta for the generic interaction model illustrated in Fig. 5.

We let \tilde{N}_A , \tilde{N}_B , and \tilde{N}_C represent the number of secondary quanta from top, middle, and bottom paths of Fig. 5(b), respectively, and $\tilde{N}_t = \tilde{N}_A + \tilde{N}_B + \tilde{N}_C$ represents the total number of secondary quanta for interaction type t . The first branch point in Fig. 5(b) represents separation (Bernoulli branch) of interacting photons that produce a fluorescent/scatter photon (paths B and C) from those that do not (path A), and Eq. (33) gives the PDF of \tilde{N}_t ,

$$p_{N_t}(N_t) = (1 - S_t)p_{N_A}(N_t|\tilde{S}_t = 0) + S_t p_{N_{B+C}}(N_t|\tilde{S}_t = 1), \quad (39)$$

where S_t represents the probability that a scatter/emission photon is generated, $p_{N_A}(N_A|\tilde{S}_t = 0)$ represents the PDF of \tilde{N}_A given no scatter/emission photon, $\tilde{N}_{B+C} = \tilde{N}_B + \tilde{N}_C$, and $p_{N_{B+C}}(N_{B+C}|\tilde{S}_t = 1)$ represents the PDF of \tilde{N}_{B+C} given a scatter/emission photon. In Secs. 2.E.1–2.E.6, we describe how to calculate $p_{N_t}(N_t)$ using the PDF-transfer approach.

2.E.1. PDF of \tilde{N}_A

The PDF of quanta from path A, $p_{N_A}(N_A|\tilde{S}_t = 0)$, is obtained from Eq. (27),

$$p_{N_A}(N_A|\tilde{S}_t = 0) = \int p_{N_{A,0}}(N_{A,0}|\tilde{S}_t = 0) \int p_{N_{A,1}}(N_{A,1}|N_{A,0}) \times p_{N_{A,2}}(N_A|N_{A,1}) dN_{A,0} dN_{A,1}, \quad (40)$$

where $p_{N_{A,0}}(N_{A,0}|\tilde{S}_t = 0) = \delta(N_{A,0} - 1)$ (the PDF of the number of quanta selected for path A given that one quantum is selected), and therefore,

$$p_{N_A}(N_A|\tilde{S}_t = 0) = \int p_{N_{A,1}}(N_{A,1}|N_{A,0} = 1) p_{N_{A,2}}(N_A|N_{A,1}) dN_{A,1}. \quad (41)$$

2.E.1.a. Conversion to secondary quanta. Conversion to electron–hole (e–h) pairs at the primary-interaction site (path A) is described using the PDF-transfer relationship for a quantum gain stage⁴³

$$p_{N_A}(N_A|\tilde{S}_t = 0) = \int p_{g_A}(N_{A,1}) p_{N_{A,2}}(N_A|N_{A,1}) dN_{A,1}, \quad (42)$$

where $p_{g_A}(N_{A,1}) = p_{g_A}(g_A)|_{g_A=N_{A,1}}$ is the PDF describing the random number of liberated e–h pairs \tilde{g}_A . We assume Poisson gain with mean $\tilde{g}_A = E/w$, where E is the incident photon energy, w is the effective energy required to liberate one e–h pair, and PDF given by Eq. (10).

2.E.1.b. Depth-dependent collection of secondary quanta. Application of an electric field across the photoconductor causes liberated e–h pairs to drift in opposite directions, generating a current that charges or discharges a capacitor. In flat-panel configurations, the collected charge may be depth dependent as e–h pairs may recombine or be trapped in the x-ray convertor.^{57,58}

We model depth-dependent charge collection as a binomial selection process (second process in path A) characterized by a Bernoulli RV having sample values 1 or 0 with probabilities that depend on interaction depth \tilde{z}_1 . We assume the average fraction of collected charges (collection efficiency) β has a depth dependence given by the Hecht relationship^{59–61}

$$\beta(z) = \frac{\lambda_e}{L} \left(1 - e^{-\frac{L-z}{\lambda_e}}\right) + \frac{\lambda_h}{L} \left(1 - e^{-\frac{z}{\lambda_h}}\right), \quad (43)$$

where L (cm) is the convertor thickness, λ_e and λ_h (cm) are mean-free drift lengths for electrons and holes, respectively, and we have assumed electrons travel toward the entrance surface and holes toward the exit surface. If charges are collected in the opposite direction, it may be necessary to exchange z and $L - z$ on the right-hand side. Low values of λ_e and/or λ_h result in fewer collected charges and potentially a secondary quantum sink.

Transfer of the PDF through depth-dependent collection processes (summarized in Table III) has recently been described,⁴² giving

$$p_{N_{A,2}}(N_A|N_{A,1}) = \int \mathcal{B}(N_A; N_{A,1}, \beta(z_1)) p_{z_1}(z_1) dz_1, \quad (44)$$

where $\mathcal{B}(N_A; N_{A,1}, \beta(z_1))$ represents the binomial distribution for $N_{A,1}$ trials and probability of success $\beta(z_1)$, and $p_{z_1}(z_1)$ represents the exponential PDF of \tilde{z}_1 . Combining the previous two results yields

$$p_{N_A}(N_A|\tilde{S}_t = 0) = \langle \mathcal{B}_A(N_A; \beta) \rangle_{z_1}, \quad (45)$$

where

$$\mathcal{B}_A(N_t; \beta) = \int \mathcal{B}(N_t; g_A, \beta(z_1)) p_{g_A}(g_A) dg_A. \quad (46)$$

The previous two results show that $p_{N_A}(N_A|\tilde{S}_t = 0)$ is equal to the binomial distribution with \tilde{g}_A trials and probability of success $\beta(\tilde{z}_1)$, averaged over all possible values of \tilde{g}_A and \tilde{z}_1 .

2.E.2. PDF of $\tilde{N}_B + \tilde{N}_C$

In the case that a characteristic/scatter photon is generated, energy may be deposited at primary and secondary absorption sites (paths B and C) as illustrated in Fig. 5. All subsequent processes may be functions of interaction depth and/or emission/scatter angle, and therefore, from Eqs. (35) and (C15), $p_{N_{B+C}}(N_{B+C}|\tilde{S}_t = 1)$ is given by

$$p_{N_{B+C}}(N_{B+C}|\tilde{S}_t = 1) = \langle p_{N_B}(N_{B+C}|\tilde{S}_t = 1, \mathbf{b}) * p_{N_C}(N_{B+C}|\tilde{S}_t = 1, \mathbf{b}) \rangle_{\mathbf{b}}, \quad (47)$$

where $\tilde{\mathbf{b}} = [\tilde{z}_1, \tilde{\theta}]$ and $\langle \cdot \rangle_{\mathbf{b}}$ represents an average over all $\tilde{\mathbf{b}}$. In Secs. 2.E.2.a–2.E.2.c, we calculate p_{N_B} and p_{N_C} for fixed $\tilde{\mathbf{b}}$ and then average over all possible values of $\tilde{\mathbf{b}}$ to get $p_{N_{B+C}}$. Averaging over $\tilde{\mathbf{b}}$ requires the joint PDF of \tilde{z}_1 and $\tilde{\theta}$, $p_{z_1, \theta}(z_1, \theta)$, described in Appendix C.

2.E.2.a. PDF of \tilde{N}_B for fixed \tilde{z}_1 and $\tilde{\theta}$. There are two processes following the cascade fork in path B of Fig. 5. The first represents conversion to e–h pairs at the primary-interaction site and the second depth-dependent charge collection. For incoherent interactions, energy deposited by the primary interaction is a function of scatter angle $\tilde{\theta}$. Therefore, from Eq. (27)

with $p_{N_{B,0}}(N_{B,0}|\tilde{S} = 1) = \delta(N_{B,0} - 1)$, p_{N_B} is given by

$$p_{N_B}(N_B|\tilde{S}_t = 1, \tilde{z}_1, \tilde{\theta}) = \int p_{N_{B,1}}(N_{B,1}|N_{B,0} = 1, \tilde{\theta}) \times p_{N_{B,2}}(N_B|N_{B,1}, \tilde{z}_1) dN_{B,1}. \quad (48)$$

Conversion to secondary quanta at primary-interaction site. The first process following the cascade fork in path B represents conversion to e-h pairs at the primary-interaction site. Therefore, similar to Eq. (42),

$$p_{N_B}(N_B|\tilde{S}_t = 1, \tilde{z}_1, \tilde{\theta}) = \int p_{g_B}(N_{B,1}; \tilde{\theta}) p_{N_{B,2}}(N_B|N_{B,1}, \tilde{z}_1) dN_{B,1}, \quad (49)$$

where $p_{g_B}(g_B; \tilde{\theta})$ represents the PDF of \tilde{g}_B for scatter angle $\tilde{\theta}$. Similar to \tilde{g}_A , we assume \tilde{g}_B is Poisson distributed with mean $\tilde{g}_B = (E - E'(\theta))/w$, where $E'(\theta)$ is the scatter/emission photon energy for angle θ .

Depth-dependent collection of secondary quanta. For fixed \tilde{z}_1 , $p_{N_{B,1}}(N_B|N_{B,1}, \tilde{z}_1)$ is given by the binomial distribution,^{42,43,62} giving

$$p_{N_B}(N_B|\tilde{S}_t = 1, \tilde{z}_1, \tilde{\theta}) = \int p_{g_B}(N_{B,1}; \tilde{\theta}) \mathcal{B}(N_B; N_{B,1}, \beta(\tilde{z}_1)) dN_{B,1}. \quad (50)$$

2.E.2.b. PDF of \tilde{N}_C for fixed \tilde{z}_1 and $\tilde{\theta}$. There are three processes following the cascade fork in path C of Fig. 3. From Eq. (27) with $p_{N_{C,0}}(N_{C,0}|\tilde{S}_t = 1) = \delta(N_{C,0} - 1)$,

$$p_{N_C}(N_C|\tilde{S}_t = 1, \tilde{z}_1, \tilde{\theta}) = \int p_{N_{C,1}}(N_{C,1}|N_{C,0} = 1, \tilde{\theta}, \tilde{z}_1) \times \int p_{N_{C,2}}(N_{C,2}|N_{C,1}, \tilde{\theta}) \times p_{N_{C,3}}(N_C|N_{C,2}, \tilde{z}_1, \tilde{\theta}) dN_{C,2} dN_{C,1}. \quad (51)$$

Reabsorption of fluorescent/scatter photon. The first process following the cascade fork in path C represents selection of fluorescent/scatter photons that are reabsorbed in the x-ray convertor material. Therefore, $p_{N_{C,1}}(N_{C,1}|N_{C,0} = 1, \tilde{\theta}, \tilde{z}_1)$ is equal to the Binomial distribution with one trial and probability of success equal to the reabsorption probability f which is a function of $\tilde{\theta}$ and \tilde{z}_1 ,

$$p_{N_{C,1}}(N_{C,1}|N_{C,0} = 1, \tilde{\theta}, \tilde{z}_1) = [1 - f(\tilde{\theta}, \tilde{z}_1)] \delta(N_{C,1}) + f(\tilde{\theta}, \tilde{z}_1) \delta(N_{C,1} - 1), \quad (52)$$

where

$$f(\tilde{z}_1, \tilde{\theta}) = \begin{cases} \int_0^{(L-\tilde{z}_1)/|\cos(\tilde{\theta})|} p_l(l) dl & 0 \leq \theta \leq \pi/2 \\ \int_0^{\tilde{z}_1/|\cos(\tilde{\theta})|} p_l(l) dl & \pi/2 < \theta \leq \pi \end{cases}, \quad (53)$$

where $p_l(l) = \mu(E_s) \exp[-\mu(E_s)l]$, where E_s represents fluorescent/scatter photon energy. Combining these expressions yields

$$p_{N_C}(N_C|\tilde{S} = 1, \tilde{z}_1, \tilde{\theta}) = [1 - f(\tilde{\theta}, \tilde{z}_1)] \int p_{N_{C,2}}(N_{C,2}|N_{C,1} = 0, \tilde{\theta}) \times p_{N_{C,3}}(N_C|N_{C,2}, \tilde{z}_1) dN_{C,2} + f(\tilde{\theta}, \tilde{z}_1) \int p_{N_{C,2}}(N_{C,2}|N_{C,1} = 1, \tilde{\theta}) \times p_{N_{C,3}}(N_C|N_{C,2}, \tilde{z}_1, \tilde{\theta}) dN_{C,2}, \quad (54)$$

where $\int p_{N_{C,2}}(N_{C,2}|N_{C,1} = 0) p_{N_{C,3}}(N_C|N_{C,2}) dN_{C,2} = \delta(N_C)$. Therefore,

$$p_{N_C}(N_C|\tilde{S} = 1, \tilde{z}_1, \tilde{\theta}) = [1 - f(\tilde{\theta}, \tilde{z}_1)] \delta(N_C) + f(\tilde{\theta}, \tilde{z}_1) \int p_{N_{C,2}}(N_{C,2}|N_{C,1} = 1, \tilde{\theta}) \times p_{N_{C,3}}(N_C|N_{C,2}, \tilde{z}_1, \tilde{\theta}) dN_{C,2}. \quad (55)$$

Conversion to secondary quanta at reabsorption site. Similar to Eqs. (42) and (49),

$$p_{N_C}(N_C|\tilde{S} = 1, \tilde{z}_1, \tilde{\theta}) = [1 - f(\tilde{\theta}, \tilde{z}_1)] \delta(N_C) + f_t(\tilde{\theta}, \tilde{z}_1) \times \int p_{g_C}(N_{C,2}; \tilde{\theta}) \times p_{N_{C,3}}(N_C|N_{C,2}, \tilde{z}_1, \tilde{\theta}) dN_{C,2}, \quad (56)$$

where $p_{g_C}(g_C; \tilde{\theta})$ represents the PDF of \tilde{g}_C for fluorescent/scatter angle $\tilde{\theta}$, where $\tilde{g}_C = E'(\theta)/w$. Similar to \tilde{g}_A and \tilde{g}_B , we assume that \tilde{g}_C is Poisson distributed.

Depth-dependent collection of secondary quanta at reabsorption site. Letting $p_{z_2}(z_2|\tilde{z}_1, \tilde{\theta})$ represent the PDF of reabsorption depth \tilde{z}_2 given \tilde{z}_1 and $\tilde{\theta}$ yields⁴²

$$p_{N_{C,3}}(N_C|N_{C,2}, \tilde{z}_1, \tilde{\theta}) = \int \mathcal{B}(N_C; g_C, \beta(z_2)) \times p_{z_2}(z_2|\tilde{z}_1, \tilde{\theta}) dz_2. \quad (57)$$

Therefore,

$$p_{N_C}(N_C|\tilde{S} = 1, \tilde{z}_1, \tilde{\theta}) = [1 - f(\tilde{\theta}, \tilde{z}_1)] \delta(N_C) + f(\tilde{\theta}, \tilde{z}_1) \int p_{g_C}(N_{C,2}; \tilde{\theta}) \times \int \mathcal{B}(N_C; g_C, \beta(z_2)) \times p_{z_2}(z_2|\tilde{z}_1, \tilde{\theta}) dz_2 dN_{C,2}. \quad (58)$$

The first term in the previous expression is a delta function at $N_C = 0$ corresponding to the event that the fluorescent/scatter photon is not reabsorbed. The second term corresponds to the event that fluorescent/scatter photon is reabsorbed.

2.E.2.c. PDF of $\tilde{N}_B + \tilde{N}_C$. Combining Eqs. (47), (50), and (58) yields

$$p_{N_{B+C}}(N_{B+C}|\tilde{S} = 1) = \langle (1 - f) \mathcal{B}_B(N_{B+C}; \beta) \rangle_{z_1, \theta} + \langle f \mathcal{B}_B \times (N_{B+C}; \beta) * \mathcal{B}_C(N_{B+C}; \beta) \rangle_{z_1, \theta}, \quad (59)$$

where $\mathcal{B}_B(N_B; \beta)$ and $\mathcal{B}_C(N_C; \beta)$ are given by

$$\mathcal{B}_B(N_i; \beta) = \int \mathcal{B}(N_i; g_B, \beta(z_1)) p_{g_B}(g_B; \theta) dg_B, \quad (60)$$

$$\mathcal{B}_C(N_i; \beta) = \int \mathcal{B}(N_i; g_C, \beta(z_2)) p_{g_C}(g_C; \theta) dg_C, \quad (61)$$

where $\mathcal{B}(N_i; g_B, \beta(z_1))$ represents the binomial distribution with g_B trials and probability of success $\beta(z_1)$, and similarly for $\mathcal{B}(N_i; g_C, \beta(z_2))$.

2.E.3. PDF of $\tilde{N}_t = \tilde{N}_A + \tilde{N}_B + \tilde{N}_C$

Combining Eqs. (39), (45), and (59) yields the PDF of the total number of quanta for interaction type t using the generic x-ray interaction model illustrated in Fig. 5,

$$p_{N_t}(N_t) = (1 - S_t) \langle \mathcal{B}_A(N_t; \beta) \rangle_{z_1} + S_t \langle (1 - f_t) \mathcal{B}_B(N_t; \beta) \rangle_{z_1, \theta} + S_t \langle f_t \mathcal{B}_B(N_t; \beta) * \langle \mathcal{B}_C(N_t; \beta) \rangle_{z_2} \rangle_{z_1, \theta}. \quad (62)$$

The average over \tilde{z}_2 in the above expression requires the PDF of \tilde{z}_2 given \tilde{z}_1 and $\tilde{\theta}$ which is derived in Appendix D. Averages over \tilde{z}_1 and $\tilde{\theta}$ require the joint PDF of \tilde{z}_1 and $\tilde{\theta}$, $p_{z_1, \theta}^t$, which for a given incident photon energy is given by⁵⁵

$$p_{z_1, \theta}^t(z_1, \theta) = p_{z_1}(z_1) p_{\theta}^t(\theta), \quad (63)$$

where p_{θ}^t depends on the interaction type and has been described in detail by Hajdok *et al.*⁶³ and Yun *et al.*^{41,47} for both photoelectric and incoherent interactions, and $p_{z_1}(z_1)$ is given by the exponential PDF $\mu(E) \exp(-\mu(E)z_1)$ normalized to unity over the convertor thickness.

The three terms in Eq. (62) describe the PDF of image quanta for (i) events that do not result in production of fluorescent/scatter x-rays, (ii) events that result in production of a fluorescent/scatter photon that escapes the detector, and (iii) events that result in production of a fluorescent/scatter photon that is reabsorbed within the detector. In Secs. 2.E.4–2.E.6, we use this result to describe the PDFs of the total number of quanta for photoelectric and incoherent interactions. Table I gives mean values and PDFs used for selection and gain variables for each interaction type, where ρ_K , ω_K , E_K , E' , w , and f_t represent the K-shell participation fraction, K-fluorescent yield, K-fluorescent photon energy, incoherent-scatter energy, average effective energy required to liberate one electron–hole pair, and scatter/emission reabsorption probability, respectively.

2.E.4. Photoelectric interactions

In a photoelectric interaction, path A of Fig. 5 corresponds to events that do not produce a fluorescent photon, and incident energy E is assumed to be absorbed at the primary-interaction site, liberating \tilde{g}_A secondaries (see Table I). Paths B and C describe events that produce a fluorescent photon,

TABLE I. Random variables and PDFs defining the type of x-ray interaction used in the generic model shown in Fig. 5.

RV	Photoelectric		Incoherent	
	Mean	PDF	Mean	PDF
\tilde{S}_t	$\omega_K \rho_K$	Bernoulli	1	δ -function
\tilde{g}_A	E/w	Poisson		
\tilde{g}_B	$(E - E_K)/w$	Poisson	$(E - E')/w$	Poisson
\tilde{g}_C	E_K/w	Poisson	E'/w	Poisson
$\tilde{\beta}_A$	$\beta(z_1)$	Bernoulli	$\beta(z_1)$	Bernoulli
$\tilde{\beta}_B$	$\beta(z_1)$	Bernoulli	$\beta(z_1)$	Bernoulli
$\tilde{\beta}_C$	$\beta(z_2)$	Bernoulli	$\beta(z_2)$	Bernoulli

resulting in \tilde{g}_B secondaries emitted locally and \tilde{g}_C liberated remotely with probability f_{pe} given by Eq. (53) with $E_s = E_K$. From Eq. (62), the PDF of \tilde{N}_{pe} is given by

$$p_{N_{pe}}(N_{pe}) = (1 - \rho_K \omega_K) \langle \mathcal{B}_A^{pe}(N_{pe}; \beta) \rangle_{z_1} + \rho_K \omega_K \langle (1 - f_{pe}) \mathcal{B}_B^{pe}(N_{pe}; \beta) \rangle_{\theta, z_1} + \rho_K \omega_K \langle f_{pe} \mathcal{B}_B^{pe}(N_{pe}; \beta) * \langle \mathcal{B}_C^{pe}(N_{pe}; \beta) \rangle_{z_2} \rangle_{\theta, z_1}, \quad (64)$$

where $p_{z_1, \theta}^{pe}$ is obtained from Eq. (63) with $p_{\theta}^{pe}(\theta) = \sin(\theta)/2$.^{38,41} The first and third terms in Eq. (64) contribute to the photopeak and the second term contributes to the K-escape peak.

2.E.5. Incoherent interactions

In an incoherent event, an incident photon interacts with a loosely bound (free) electron producing a Compton-scatter photon and recoil electron. The energy of the scatter photon E' is a function of both incident photon energy and scatter polar angle θ , $E' = E/(1 + \alpha(1 - \cos(\theta)))$, where $\alpha = E/m_0 c^2$ represents the incident photon energy in units of electron rest-mass energy ($m_0 c^2 = 511$ keV).⁶⁴ The recoil electron deposits its energy at the primary-interaction site with mean conversion gain $\tilde{g}_B = (E - E')/w$. The scatter photon is reabsorbed with probability f_{inc} given by Eq. (53). From Eq. (62), the PDF of \tilde{N}_{inc} is given by

$$p_{N_{inc}}(N_{inc}) = \langle (1 - f_{inc}) \mathcal{B}_B^{inc}(N_{inc}; \beta) \rangle_{\theta, z_1} + \langle f_{inc} \mathcal{B}_B^{inc}(N_{inc}; \beta) * \langle \mathcal{B}_C^{inc}(N_{inc}; \beta) \rangle_{z_2} \rangle_{\theta, z_1}, \quad (65)$$

where $p_{z_1, \theta}^{inc}$ is given by Eq. (63) with $p_{\theta}^{inc}(\theta)$ described in detail by Hajdok *et al.*⁶³ and Yun *et al.*^{41,47} The first term in Eq. (65) represents the distribution of secondaries collected from energy deposition by the recoil electron and the second term contributes to the photopeak.

2.E.6. PDF of detector element signal \tilde{d}

Combining Eqs. (38), (64), and (65) yields the PDF of $\tilde{N}_{tot} = \tilde{N}_{pe} + \tilde{N}_{inc}$,

$$p_{N_{tot}}(N_{tot}) = \bar{\xi}_{pe} (1 - \rho_K \omega_K) \langle \mathcal{B}_A^{pe}(N_{tot}; \beta) \rangle_{z_1} + \bar{\xi}_{pe} \rho_K \omega_K \langle (1 - f_{pe}) \mathcal{B}_B^{pe}(N_{tot}; \beta) \rangle_{\theta, z_1} + \bar{\xi}_{pe} \rho_K \omega_K \langle f_{pe} \mathcal{B}_B^{pe}(N_{tot}; \beta) * \langle \mathcal{B}_C^{pe}(N_{tot}; \beta) \rangle_{z_2} \rangle_{\theta, z_1} + \bar{\xi}_{inc} \langle (1 - f_{inc}) \mathcal{B}_B^{inc}(N_{tot}; \beta) \rangle_{\theta, z_1} + \bar{\xi}_{inc} \langle f_{inc} \mathcal{B}_B^{inc}(N_{tot}; \beta) * \langle \mathcal{B}_C^{inc}(N_{tot}; \beta) \rangle_{z_2} \rangle_{\theta, z_1}. \quad (66)$$

The PDF of \tilde{d} given interacting photon energy E including electronic readout noise is obtained by convolving Eq. (37) with the electronic noise PDF,^{42,43}

$$p_d(d|E) = \frac{1}{k} p_{N_{tot}}(d/k) * p_e(d), \quad (67)$$

where $p_{N_{tot}}(d/k) = p_{N_{tot}}(N_{tot})|_{\tilde{N}_{tot}=d/k}$ and $p_e(d)$ describes the zero-mean distribution of (postbinning) detector readout

noise and k is a constant of proportionality converting a number of quanta to the detector-element signal.

Equations (66) and (67) describe the PDF of element signals after adaptive binning prior to thresholding for single-Z detector materials. A description of multi-Z SPC detector materials, such as CdTe and CdZnTe, requires the evaluation of Eq. (66) for each atom type and potentially terms that account for emission of characteristic photons from the lower Z atoms (e.g., Cd) following reabsorption of characteristic photons emitted from the higher Z atoms (e.g., Te).⁴⁷

The response function R , which represents the probability density of estimated photon energy ε given interacting photon energy E , is given by

$$R(\varepsilon|E) = \frac{1}{\kappa} p_d(d|E)|_{d=\varepsilon/\kappa} \quad (68)$$

$$= \frac{1}{k\kappa} p_{N_{\text{tot}}}(\varepsilon/k\kappa) * p_e(\varepsilon/\kappa), \quad (69)$$

where κ is a constant of proportionality converting a detector-element signal to estimated photon energy.

To illustrate the utility of this theoretical formalism, we use the previous three expressions with Eqs. (1) and (3) to calculate the zero-frequency DQE of Si-based SPC detectors, such as the MEDIPIX prototypes,^{1,4,29,65,66} and a hypothetical Se-based SPC detector that implements adaptive element binning. While Se is not currently used in photon-counting x-ray imaging, applying the developed formalism to Se is useful in illustrating the potentially degrading effects that escape of characteristic x-rays may have on photon-counting image quality.

2.F. Frequency-dependent DQE

A simple estimate of the DQE frequency dependence comes from recognizing that, assuming ideal adaptive binning, the primary interaction location is known to be somewhere within the detector element of width a at the center of the binned region, resulting in a sinc-shaped MTF. In addition, due to noise aliasing caused by sampling at locations corresponding to the center of detector elements, the Wiener NPS will be uniform³⁶ with frequency up to the sampling cutoff frequency, resulting in a DQE given by

$$\text{DQE}(u) = \text{DQE}(0) \text{sinc}^2(\pi au). \quad (70)$$

Charge sharing in the detector might enable the primary interaction to be located with subelement resolution, resulting in even better MTF and DQE performance. While these results may be achieved at energies below the detector K-edge energy (e.g., mammography energies), they may not be achieved if the primary-interaction site cannot be identified correctly, such as when more energy is deposited by reabsorption of a scatter photon than by the primary interaction.

3. MONTE CARLO (MC) COMPARISON

Predictions of this CSA approach were compared with a MC study of the DQE of Si- and Se-based SPC detectors that implement adaptive binning. Simulations were performed

TABLE II. Material properties for α -Se and Si.

	Symbol	Se	Si
Mass density (g cm ⁻³)	ρ	4.3	2.3
K-fluorescent energy (Ref. 64) (keV)	E_K	11.2	1.7
K-shell participation fraction (Ref. 64)	ρ_K	0.864	0.904
K-fluorescence yield (Ref. 64)	ω_K	0.589	0.054
Average ionization energy (Ref. 67) (eV)	w	45	3.62

in three stages: (1) energy deposition, (2) charge liberation and collection, and (3) adaptive binning, electronic noise, and thresholding. Table II summarizes physical parameters used in combination with the physical models described in Sec. 2.E.

3.A. Energy deposition

Energy deposition was simulated using the particle tracking (pTrac) function of the MC user code `mcnp5`TM. Energy-deposition data were collected in list mode, giving three-dimensional (3D) positions and energies of energy-deposition events following each primary photon interaction. Simulations were performed for uniformly distributed photon fluences and $2000 \times 2000 \times 10 \times 10 \mu\text{m}^2$ scoring bins. In all cases, ranges of photoelectrons and Compton recoil electrons were not considered (i.e., site of charge liberation is the same as x-ray interaction). Double (or triple) counting of incident photons caused by the finite range of photoelectrons and Compton recoil electrons was therefore not considered in this analysis. In addition, we assumed count rates low enough that pulse pileup effects could be ignored. A similar MC technique was implemented by Yun *et al.*⁴¹ for the description of conventional energy-integrating detectors and the reader is referred there for more details.

3.B. Charge liberation and collection

In all cases, we assume that the site of charge collection is the same as charge liberation, i.e., no charge diffusion. This may be a reasonable assumption for larger adaptively binned elements and higher threshold levels where the number of double-counting events caused by partial energy absorption in neighboring elements is reduced, as discussed by Xu *et al.*⁶⁸ and Lundqvist *et al.*,¹⁶ respectively, but represents an optimistic estimate of detector performance for smaller element sizes.

Charge liberation. Liberation of e-h pairs was simulated by sampling a Poisson distribution with mean value E_{dep}/w for each photon interaction, where E_{dep} represents deposited photon energy (obtained from the previous stage). The output of this stage was the 3D position and number of liberated e-h pairs for each energy-deposition event.

Charge collection. We simulated collection of liberated charges by sampling a binomial distribution with number of trials equal to the number of liberated e-h pairs and depth-dependent probability of success $\beta(z)$ given by the Hecht

relation [Eq. (43)]. We consider two extreme cases of charge collection: asymmetric and symmetric collection of charge carriers. In the case of Se, we consider an asymmetric case and assume the mean-free drift length for electrons (λ_e) is two orders of magnitude lower than that for holes.⁶¹ In the case of Si, consider a symmetric case and assume mean-free drift lengths of holes and electrons are of the same order of magnitude. Calculations were performed for each energy-depositing event, giving the 2D position and number of collected e-h pairs for each primary and secondary photon interaction.

3.C. Adaptive binning, electronic noise, and thresholding

We simulated two types of adaptive binning. For the first type, which represents an ideal situation, we summed e-h pairs collected from primary- and secondary-reabsorption sites and then added a sample from a zero-mean Gaussian distribution to simulate electronic noise. When the resulting signal was above the threshold level, a count was attributed to the element with the highest detected charge.

For the second type of adaptive binning, which is similar to that implemented in MEDIPIX Si-based detectors,⁴ we added electronic noise (σ_e^{pb}) to each prebinning detector element, clustered elements into larger $n \times n$ elements, and then summed charges collected from all interactions within each cluster. When the signal from a cluster was above the threshold level, a count was attributed to the element (within the cluster) with the highest detected charge.

Each adaptive-binning approach was performed for prebinning element areas of $100 \times 100 \mu\text{m}^2$ and a threshold equal to three times the electronic noise level (σ_e) of adaptively binned signals. This resulted in a $2 \times 2 \text{ cm}^2$ SPC image from which DQE(0) was determined.

3.D. DQE calculation

We calculated DQE(0) from MC images using the following relationship:

$$\text{DQE}(0) = \alpha \frac{\text{SNR}_{\text{meas}}^2}{\text{SNR}_{\text{ideal}}^2} = \frac{\text{SNR}_{\text{meas}}^2}{\bar{q}_0 a}, \quad (71)$$

where SNR_{meas} and $\text{SNR}_{\text{ideal}} (= \alpha \bar{q}_0 a)$ represent the measured and ideal SPC signal-to-noise ratio, respectively, and α represents the quantum efficiency.

4. RESULTS

4.A. PDF of detector element signals, $p_d(d|E)$

Figure 6 illustrates $p_{N_{\text{tot}}}(N_{\text{tot}})$ for Se and Si convertor materials for the model illustrated in Fig. 4 calculated for selected photon energies, convertor thicknesses, and mean-free drift lengths for holes. For systems that implement adaptive element binning, $p_{N_{\text{tot}}}$ is related to p_d through Eq. (67). Figure 6 shows good agreement between theoretical and MC simulations for all conditions considered.

In general, for both Se and Si, low mean-free drift lengths ($\sim 0.1 \text{ cm}$) result in broad and asymmetric photopeaks that are shifted toward lower energies due to depth-dependent collection efficiencies. This effect is more severe for thicker convertor materials, where the collection efficiency has a stronger depth dependence,^{59–61} and for higher energy photons, where the distribution of interaction depths is more uniform. Although not shown in Fig. 6, electronic noise results in further photopeak broadening. For systems with sufficiently low electronic noise levels and high mean-free drift lengths (i.e., $\lambda_h \gg L$), stochastic energy deposition and conversion processes are primary causes of spectral distortion, resulting in finite-width photopeaks, K-escape peaks,

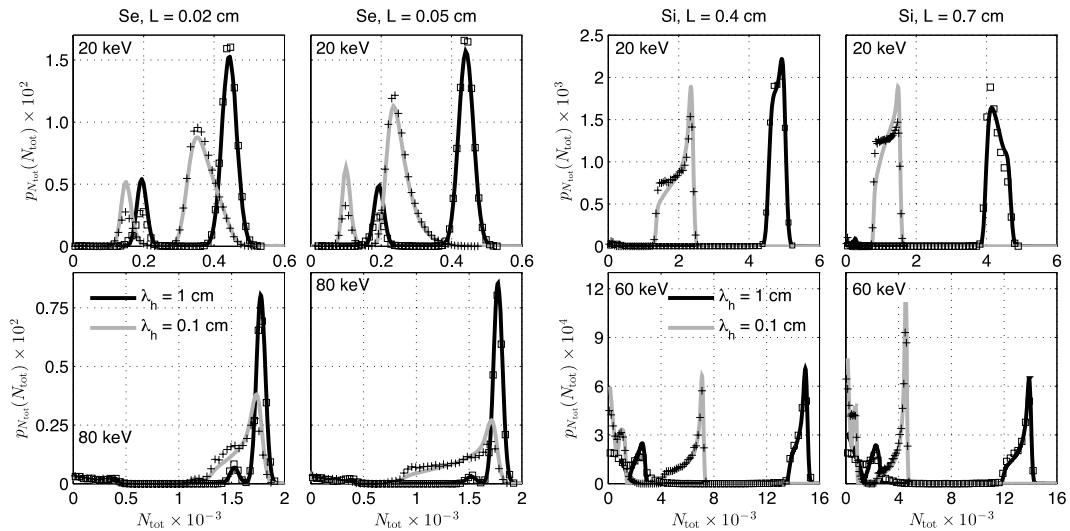


FIG. 6. PDFs of the total number of quanta collected by detector elements for selected photon energies for (left) Se- and (right) Si-based convertor materials for selected mean-free drift lengths for holes (λ_h). Calculations for Se assumed asymmetric charge collection (i.e., $\lambda_e \ll \lambda_h$). Calculations for Si assumed symmetric charge collection (i.e., $\lambda_e \sim \lambda_h$). Curves and symbols represent theoretical and Monte Carlo data, respectively.

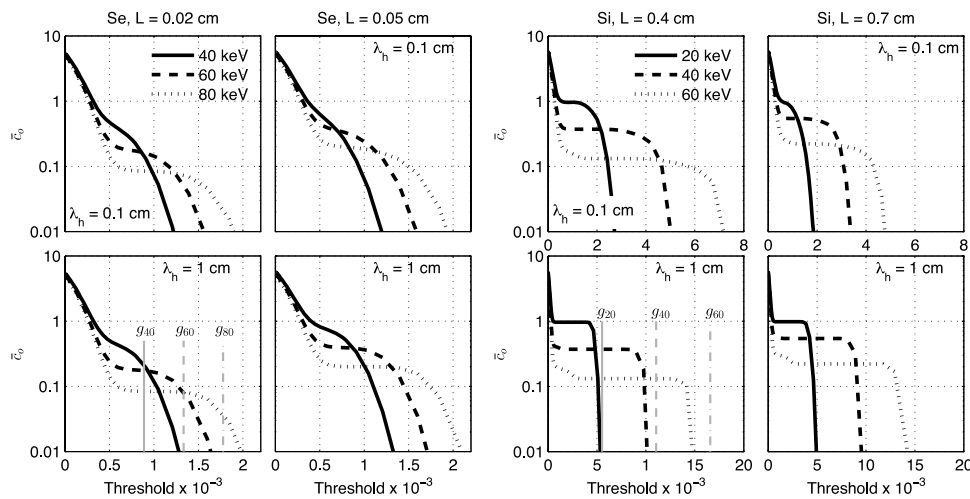


FIG. 7. Normalized SPC pixel value \bar{c}_0 (counts per incident photon) as a function of threshold t for selected Se and Si convertor thicknesses with $\sigma_e = 200$ e-h pairs and $\lambda = 1/10$. Vertical gray lines indicate mean conversion gains for the indicated energies. Calculations for Se assumed asymmetric charge collection (i.e., $\lambda_e \ll \lambda_h$). Calculations for Si assumed symmetric charge collection (i.e., $\lambda_e \sim \lambda_h$).

and a distribution of low-energy deposition events with area determined by the Compton cross section.

4.B. Optimal SPC threshold

Figure 7 illustrates the dependence of normalized SPC pixel value ($\bar{c}/\bar{q}_0 a$) on threshold level for selected Se and Si convertor thicknesses, photon energies, and mean-free drift lengths. All curves in Fig. 7 were calculated assuming $\sigma_e = 200$ e-h pairs and small $\lambda (=1/10)$ such that pulse pileup could be ignored.

For both Se and Si, as expected, threshold values lower than approximately $3\sigma_e$ result in an inflated image signal due to false electronic noise counts. For threshold values greater than $3\sigma_e$, a plateau is reached with height approximately equal to the quantum efficiency. Width of the plateau depends on the number of secondaries collected per interacting x-ray photon and, in general, is narrower for lower energy photons than for higher energy photons and for materials with higher w values (such as Se). Decreasing the mean-free drift length

of holes and electrons results in fewer collected secondaries which results in a secondary quantum sink and narrowing of the range of acceptable threshold values.

4.C. Zero-frequency DQE of SPC detectors

Figure 8 illustrates the dependence of DQE(0) on incident photon energy for selected Se and Si convertor thicknesses and mean-free drift lengths. In all cases, we have assumed $t = 3\sigma_e$, $\lambda \ll 1$, and ideal adaptive binning described in Sec. 3.C. Good agreement between theoretical and MC results is observed for all conditions considered.

At fluoroscopic and radiographic energies (>40 keV), DQE(0) for Se is approximately equal to the quantum efficiency for all convertor thicknesses, mean-free drift lengths, and electronic noise levels considered. However, for higher levels of electronic noise and mammographic photon energies (<40 keV), DQE(0) for Se is degraded substantially due to loss of energy-deposition events below the electronic noise floor ($3\sigma_e$). This effect is caused by a combination of

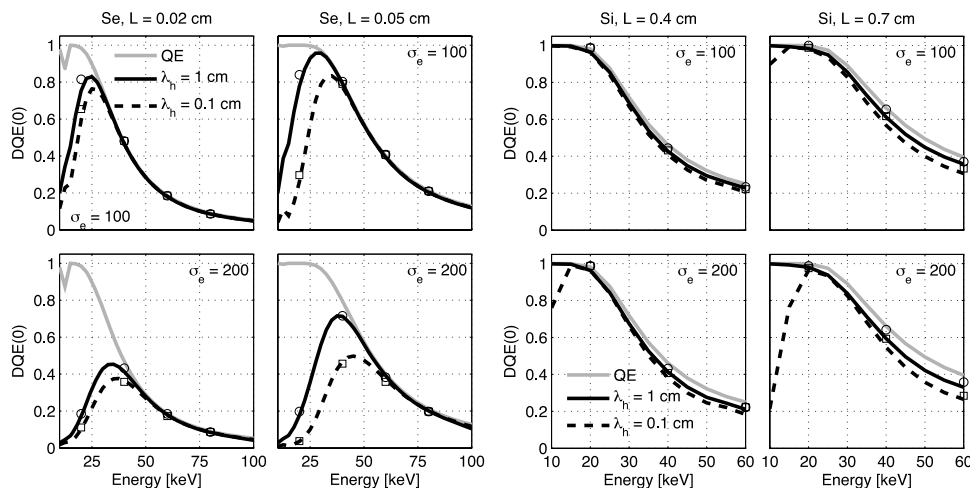


FIG. 8. DQE(0) as a function of incident photon energy for selected (left) Se and (right) Si convertor thicknesses, mean-free drift lengths, and electronic noise levels. Lines and symbols represent theoretical and Monte Carlo data, respectively. The gray curve indicates the quantum efficiency.

low gain at lower energies, poor collection efficiency, and thresholding.

In the case of Si for $E \leq 20$ keV, DQE(0) is degraded by high electronic noise and poor collection efficiency. For higher (30–60 keV) energies and thicker convertor materials, there is a slight DQE reduction that is likely due to the combination of lower charge collection and an increase in the number of Compton interactions that together result in more events below the electronic noise floor.

4.D. Effect of adaptive binning on image SNR

Figure 9 illustrates the dependence of $\text{SNR}^2/\alpha\bar{q}_0a$ on pre-binning additive noise level (σ_e^{pb}) for Se- and Si-based systems. Monte Carlo results were calculated assuming 2×2 and 10×10 binned elements. Theoretical results were calculated assuming ideal adaptive binning described in Sec. 3.C with additive noise levels equal to $2\sigma_e^{\text{pb}}$ and $10\sigma_e^{\text{pb}}$ for 2×2 and 10×10 cases, respectively. In all cases, a threshold of $t \geq 3 \times n\sigma_e^{\text{pb}}$ ($n = 2, 10$) was implemented. A value of $\text{SNR}^2/\alpha\bar{q}_0a = 1$ represents the ideal situation where image SNR is not degraded by stochastic deposition, liberation, or collection processes, or electronic noise.

Figure 9 illustrates the expected result that as the number of binned elements is increased, image SNR decreases due to an increase in additive noise. In the case of Se, with the exception of the 2×2 case for $\sigma_e^{\text{pb}} \lesssim 60$, there is good agreement between MC and theory. Disagreement for 2×2

elements and $\sigma_e^{\text{pb}} \lesssim 60$ is likely the result of a characteristic photon escaping from the binned element surrounding the primary interaction and causing an additional count in a neighboring binned element. This “double counting” results in an inflated image signal and a misleading increase in SNR that is not accounted for in the theoretical model. This effect disappears for $\sigma_e^{\text{pb}} \gtrsim 60$ because thresholds t (≥ 360 e–h pairs) are higher than the signal (≈ 250 e–h pairs) generated by reabsorbed fluorescent photons.

A similar discrepancy between theory and MC is observed for Si. In the case of Si, this discrepancy may be due to re-absorption of Compton-scatter x-rays. Since Compton-scatter x-rays can retain a large fraction of incident photon energy, increasing the threshold does not reduce the number of double counts.

5. DISCUSSION

A theoretical framework is presented for obtaining the energy-response function of photon-counting x-ray detectors. This was made possible by introducing new relationships that describe propagation of the PDF of the total number of image-forming quanta through complicated parallel cascades of image-forming processes for photon-counting x-ray detectors. This is required when there is more than one image-forming process that contributes to an image signal, such as in the case of reabsorption of fluorescent and Compton-scatter photons. Using this approach, the zero-frequency DQE and average count rate of hypothetical silicon- and selenium-based SPC detectors were determined including the effects of escape and reabsorption of fluorescent and Compton-scatter photons, stochastic conversion to secondary quanta, depth-dependent charge collection, and electronic noise.

For photon-counting systems that implement adaptive element binning, the zero-frequency DQE is equal to the quantum efficiency multiplied by a new SPC noise factor, I_{SPC} . This term is equal to the probability of counting a photon given an interaction event, i.e., the true-positive fraction of photon counts, and has the appearance of a “photon-counting” Swank-noise factor.

The CSA model of I_{SPC} based on a generalized depth-dependent interaction model incorporating the statistics of liberation and collection of secondary quanta showed that the DQE is degraded by escape of fluorescent and Compton-scatter photons, depth-dependent collection efficiency, and electronic noise. It was demonstrated that for Si- and Se-based SPC systems, there is a narrow range of acceptable thresholds that depends on photon energy, collection efficiency, and electronic noise level. Thresholds that adequately suppress electronic noise without thresholding out interaction events will provide a DQE that is approximately equal to the quantum efficiency. In this case, as expected, the DQE is not compromised by Swank noise or electronic noise. However, in some cases, this condition may not be satisfied, such as at lower mammographic energies, higher levels of electronic noise, or poor collection efficiencies. Under these conditions, our results suggest that Si detectors that liberate more charges per interacting x-ray photon will achieve superior DQE performance.

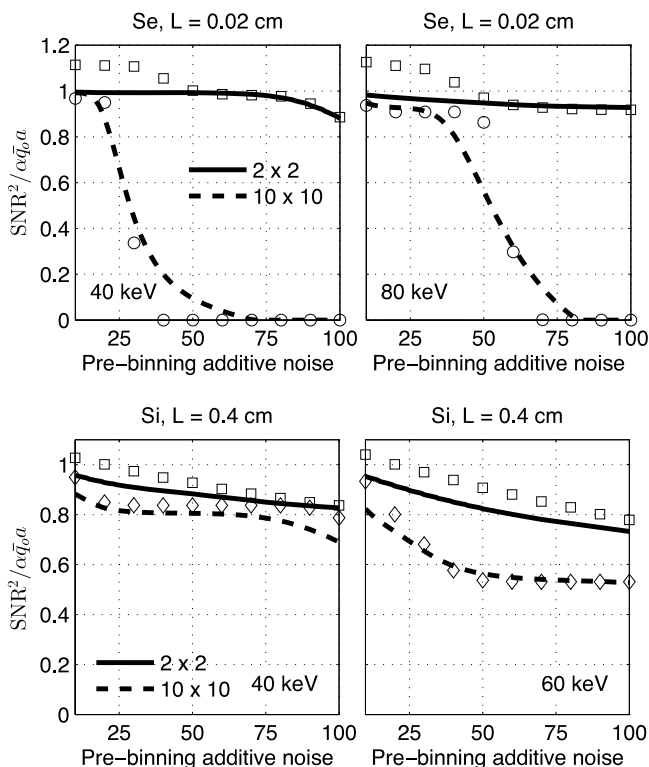


FIG. 9. $\text{SNR}^2/\alpha\bar{q}_0a$ as a function of additive noise for selected photon energies incident on Se and Si detectors that implement adaptive binning. Theoretical curves are calculated assuming “ideal” adaptive binning with additive noise σ_e equal to n ($n = 2, 10$) times the prebinning electronic noise.

In all cases, our theoretical models assumed an adaptive binning approach where all interacting photon energy was assumed to be collected in a single large element. Comparison with MC simulations showed that this can be good approximation to systems that cluster elements into $n \times n$ larger elements, then sum charge collected from all interactions within each cluster and attribute a count to the element (within a cluster) with the largest detected charge. For example, our theoretical model agreed very well with MC predictions of the DQE of Se-based systems that cluster elements into $200 \times 200 \mu\text{m}^2$ binned elements and applies a threshold that eliminates double counts caused by reabsorption of fluorescent photons. For sufficiently low electronic noise levels, loss of signal generated by thresholding out reabsorbed fluorescent photons has negligible effect on the DQE. Similar trends and agreement were observed for Si-based systems, although our results suggest that larger ($>200 \times 200 \mu\text{m}^2$) binned elements may be required to adequately suppress double counting reabsorbed Compton-scattered x-rays.

Furthermore, our Monte Carlo analysis illustrates that uncorrected double (or triple) counting of interacting photons may result in a misleading increase in image SNR (and therefore DQE) of SPC systems. This effect will be more severe when charge sharing caused by charge diffusion and electron transport, which were not modeled in either theoretical or MC analyses, is considered. We suspect this apparent increase may be due to nonlinear relationships between reabsorption, thresholding, and image noise, although such a relationship was not considered in detail in this study. In the future, it will be essential to quantify such relationships to avoid potentially over estimating the DQE of SPC systems.

In this paper, results have been compared with Monte Carlo simulations only for single-Z detector materials. Multi-Z detector materials have the potential to differ slightly from single-Z models when the characteristic emission from a high-Z atom interacts with a lower Z atom to create a new lower energy characteristic emission. The impact of this is known to be minimal with conventional energy-integrating CsI detectors where the two atoms have very similar atomic numbers, but is less clear with some SPC detectors such as CdZnTe.

6. CONCLUSIONS

A method of describing the zero-frequency DQE of photon-counting x-ray imaging detectors, including the effects of reabsorption of characteristic and Compton-scatter photons in a convertor material, is described. This approach uses the concepts of cascaded-systems analysis to determine the PDF of the total number of image-forming quanta resulting from parallel image-forming processes, such as energy deposition at primary-interaction and reabsorption sites. The model demonstrated good agreement with a Monte Carlo simulation of Si- and Se-based detectors under a realistic range of parameters. Application of this PDF-transfer approach shows that low conversion gain, depth-dependent collection efficiency, high electronic noise, and escape of

characteristic/scatter photons can result in degradation of the photon-counting DQE under some conditions and provides a framework for the development of high-performance photon-counting and energy-resolving x-ray systems.

APPENDIX A: LIST OF VARIABLES

In the following, overhead $\tilde{\cdot}$ indicates a random variable, p_x represents the PDF of the variable \tilde{x} , and $p_{x,y}$ represents the joint PDF of \tilde{x} and \tilde{y} .

Symbol	Definition
\bar{c}	Mean SPC image signal.
ε	Estimated photon energy.
$R(\varepsilon, E)$	Response function of SPC detectors.
ζ	Probability of observing a false count due to electronic noise.
λ	Mean number of photons incident on one adaptively binned element during a single integration period.
$\tilde{g}, p_g(g)$	Conversion gain (and associated PDF).
$\text{pr}_g(g)$	PMF of discrete conversion gain variable \tilde{g} .
$\tilde{N}_i, p_{N_i}(N_i)$	Total number of secondary quanta (and associated PDF) after the i th stage of a serial cascade of quantum processes.
$p_{N_i}(N_i N_{i-1})$	PDF of the total number of secondary quanta after the i th stage of a serial cascade of quantum processes given N_{i-1} quanta after the $(i-1)$ th stage.
$\tilde{N}_{A+B}, p_{N_{A+B}}(N_{A+B})$	Total number of quanta (and associated PDF) from parallel paths A and B.
$p_{N_A N_B}(N_A, N_B)$	Joint PDF of the total number of quanta from parallel paths A and B.
$p_{N_{A,B}}(N_A, N_B \tilde{N}_0)$	Joint PDF of the total number of quanta from parallel paths A and B given \tilde{N}_0 input quanta.
$\tilde{\xi}_{j,A}$	Bernoulli RV describing selection of the i th quanta to follow path A of a parallel cascade.
$p_{\xi_{j,A}\xi_{j,B}}(\xi_{j,A}\xi_{j,B})$	Joint PDF of Bernoulli RVs $\tilde{\xi}_{j,A}$ and $\tilde{\xi}_{j,B}$.
$p_{N_A}(N_A \tilde{\xi}_A)$	PDF of \tilde{N}_A given $\tilde{\xi}_A$.
$\tilde{N}_{A,i}$	Total number of quanta after the i th elementary process of path A.
$p_{N_{A,i}}(\tilde{N}_{A,i} \tilde{N}_{A,i-1})$	PDF of $\tilde{N}_{A,i}$ given $\tilde{N}_{A,i-1}$.
$\tilde{N}_{\text{tot}}, p_{N_{\text{tot}}}(N_{\text{tot}})$	Total number of collected secondaries per x-ray interaction and associated PDF.
$p_{N_{\text{tot}}}^{\text{PPU}}(N_{\text{tot}})$	PDF of the total number of secondary quanta collected per integration period including the effects of pulse pileup.
$\tilde{d}, p_d(d E)$	PDF of adaptively binned element signal \tilde{d} given photon energy E .
$\tilde{N}_t, p_{N_t}(N_t)$	Total number of quanta (and associated PDF) for interaction of type t .
$\mathcal{B}(N_t; g, \beta)$	Binomial distribution for g trials and probability of success β , evaluated at N_t .

$\mathcal{B}_X(N_i; \beta)$ Binomial distribution for probability of success β averaged over all possible gain values (\tilde{g}_X) of path X , evaluated at N_i .

APPENDIX B: PDF TRANSFER THROUGH ELEMENTARY QUANTUM PROCESSES

A summary of PDF-transfer relationships describing how the PDF of the total number of image quanta is passed through elementary gain stages including both input-labeled and noninput-labeled stages, derived previously,^{42,43} is summarized in Table III. Combining Eqs. (B1) and (B2), (B3) or (B4) yields the transfer relationship for a quantum selection process. Combining Eqs. (B1) and (B5), (B6), or (B7) yields the transfer relationship for a quantum selection process.

APPENDIX C: JOINT PDF OF PARALLEL PROCESSES

1. Joint PDF and branch points

Random selection of quanta from an input distribution (Fig. 2) is characterized by Bernoulli RVs $\tilde{\xi}_{j,A}$ and $\tilde{\xi}_{j,B}$ with sample values of 1 and 0 corresponding to selection, or not, of the j th quantum. We let $\tilde{\xi}_A = [\tilde{\xi}_{A,1} \dots \tilde{\xi}_{A,\tilde{N}_0}]$ (and similarly for path B). From Eq. (20), the joint PDF of \tilde{N}_A and \tilde{N}_B given \tilde{N}_0 , $\tilde{\xi}_A$, and $\tilde{\xi}_B$ is given by

$$p_{N_{A,B}}(N_A, N_B | \tilde{N}_0, \tilde{\xi}_A, \tilde{\xi}_B) = \delta \left(N_A - \sum_{j=1}^{\tilde{N}_0} \tilde{\xi}_{j,A}, N_B - \sum_{j=1}^{\tilde{N}_0} \tilde{\xi}_{j,B} \right), \quad (\text{C1})$$

TABLE III. Summary of PDF transfer relationships through elementary gain and selection processes (Refs. 42 and 43).

Process	PDF-transfer relationships	PDF transfer
General gain or selection		
		(B1)
	Conditional PDF for quantum processes	
Quantum selection (Ref. 43)		(B2)
Input-labeled quantum selection I: one set of parameters \mathbf{b} for <i>all</i> input quanta (Ref. 42)		(B3)
Input-labeled quantum selection II: one set of parameters \mathbf{b}_j for <i>each</i> input quantum (Ref. 42)		(B4)
Quantum gain (Ref. 43)		(B5)
Input-labeled quantum gain I: one set of parameters \mathbf{b} for <i>all</i> input quanta (Ref. 42)		(B6)
Input-labeled quantum gain II: one set input parameters \mathbf{b}_j for <i>each</i> input quantum (Ref. 42)		(B7)

where δ denotes the 2D Dirac δ function. Using the δ -function translation property gives

$$p_{N_{A,B}}(N_A, N_B | \tilde{N}_0, \tilde{\xi}_A, \tilde{\xi}_B) = \left[\delta(N_A - \tilde{\xi}_{A,1}, N_B - \tilde{\xi}_{B,1}) * \dots * \delta(N_A - \tilde{\xi}_{A,\tilde{N}_0}, N_B - \tilde{\xi}_{B,\tilde{N}_0}) \right] \quad (C2)$$

where $*$ represents the convolution operator, and

$$p_{N_{A,B}}(N_A, N_B | \tilde{N}_0) = \left[\int \delta(N_A - \tilde{\xi}_{A,1}, N_B - \tilde{\xi}_{B,1}) p_{\xi_A, \xi_B}(\xi_{A,1}, \xi_{A,1}) d\xi_{A,1} d\xi_{B,1} \right] * \dots * \left[\int \delta(N_A - \tilde{\xi}_{A,\tilde{N}_0}, N_B - \tilde{\xi}_{B,\tilde{N}_0}) p_{\xi_A, \xi_B}(\xi_{A,\tilde{N}_0}, \xi_{B,\tilde{N}_0}) d\xi_{A,\tilde{N}_0} d\xi_{B,\tilde{N}_0} \right] \quad (C4)$$

and the δ -function sifting property results in Eq. (21).

2. Joint PDF following parallel cascades

Assuming that processes in path A are independent of those in path B, the joint PDF of $\tilde{N}_{j,A}$ ($=\tilde{N}_{j,A,n_A}$) and $\tilde{N}_{j,B}$ ($=\tilde{N}_{j,B,n_B}$) in Eq. (28) is given by

$$p_{N_{j,A,B}}(N_{j,A}, N_{j,B} | \tilde{\xi}_{j,A}, \tilde{\xi}_{j,B}) = p_{N_{j,A}}(N_{j,A} | \tilde{\xi}_{j,A}) p_{N_{j,B}}(N_{j,B} | \tilde{\xi}_{j,B}). \quad (C5)$$

Each trial is independent, giving

$$p_{\{N_{j,A}, N_{j,B}\}}(\{N_{j,A}, N_{j,B}\} | \tilde{N}_0, \tilde{\xi}_A, \tilde{\xi}_B) = \prod_{j=1}^{\tilde{N}_0} \prod_{j'=1}^{\tilde{N}_0} p_{N_{j,A}}(N_{j,A} | \tilde{\xi}_{j,A}) p_{N_{j',B}}(N_{j',B} | \tilde{\xi}_{B,j'}) \quad (C6)$$

and the joint PDF of \tilde{N}_A and \tilde{N}_B is therefore given by

$$p_{N_{A,B}}(N_A, N_B | \tilde{N}_0, \tilde{\xi}_A, \tilde{\xi}_B) = p_{N_A}(N_A | \tilde{N}_0, \tilde{\xi}_A) p_{N_B}(N_B | \tilde{N}_0, \tilde{\xi}_B), \quad (C7)$$

where

$$p_{N_A}(N_A | \tilde{N}_0, \tilde{\xi}_A) = p_{N_{1,A}}(N_A | \tilde{\xi}_{1,A}) * \dots * p_{N_{\tilde{N}_0,A}}(N_A | \tilde{\xi}_{\tilde{N}_0,A}) \quad (C8)$$

and similarly for path B. Combining these results yields

$$p_{N_{A,B}}(N_A, N_B | \tilde{N}_0, \tilde{\xi}_A, \tilde{\xi}_B) = \left[p_{N_{1,A}}(N_A | \tilde{\xi}_{1,A}) p_{N_{1,B}}(N_B | \tilde{\xi}_{1,B}) \right] * \dots * \left[p_{N_{\tilde{N}_0,A}}(N_A | \tilde{\xi}_{\tilde{N}_0,A}) p_{N_{\tilde{N}_0,B}}(N_B | \tilde{\xi}_{\tilde{N}_0,B}) \right]. \quad (C9)$$

Since $\{\tilde{N}_{j,A}, j = 1.. \tilde{N}_0\}$ are identically distributed RVs,

$$p_{N_{A,B}}(N_A, N_B | \tilde{N}_0, \tilde{\xi}_A, \tilde{\xi}_B) = \left[p_{N_{A,1}}(N_A | \tilde{\xi}_A) p_{N_{B,1}}(N_B | \tilde{\xi}_B) \right] *^{\tilde{N}_0-1} \left[p_{N_{A,1}}(N_A | \tilde{\xi}_A) p_{N_{B,1}}(N_B | \tilde{\xi}_B) \right], \quad (C10)$$

$$p_{N_{A,B}}(N_A, N_B | \tilde{N}_0) = \int \dots \int p_{N_{A,B}}(N_A, N_B | \tilde{N}_0, \tilde{\xi}_A, \tilde{\xi}_B) \times p_{\xi_A, \xi_B}(\xi_A, \xi_B) d^{\tilde{N}_0} \xi_A d^{\tilde{N}_0} \xi_B, \quad (C3)$$

where p_{ξ_A, ξ_B} represents the joint PDF of $\{\tilde{\xi}_{j,A}, \tilde{\xi}_{j,B}, j = 1.. \tilde{N}_0\}$, and $\int d^{\tilde{N}_0} \xi$ represents an \tilde{N}_0 -dimensional integral with respect to ξ . Each trial is independent of all others,⁵⁵ giving

where $p_{N_{A,1}}$ represents the PDF of \tilde{N}_A for any one quantum input to the parallel cascade, with a similar result for path B, and is equal to the 2D convolution of the first square brackets with itself $\tilde{N}_0 - 1$ times. Averaging over $\tilde{\xi}_A$ and $\tilde{\xi}_B$ yields Eq. (29).

3. Joint PDF of coupled input-labeled parallel cascades

In many situations, parameters describing individual processes (gain or selection in Fig. 3) are themselves functions of some RV associated with each quantum input to that process, called input-labeled random processes.⁵⁶ Here, we generalize the previous result for input-labeled random processes in each parallel cascade, and in particular when labels on individual input quanta may affect several processes.

We let $\tilde{\mathbf{b}}_j = [\tilde{b}_{j,1}, \tilde{b}_{j,1}, \dots, \tilde{b}_{j,m}]$ be a $1 \times m$ random vector with components representing input parameters associated with the j th input quantum. For example, in the case of photoelectric interactions, the characteristic-reabsorption probability depends on both $\tilde{\theta}$ and \tilde{z}_1 and therefore $m = 2$. We represent the joint PDF of $\tilde{b}_{j,1}, \tilde{b}_{j,1}, \dots, \tilde{b}_{j,m}$ as $p_{\mathbf{b}}(\mathbf{b}_j) = p_{\mathbf{b}}(b_{j,1}, b_{j,2}, \dots, b_{j,m})$. It is also true that for a fixed set of parameters ($\tilde{\xi}$ and $\tilde{\mathbf{b}}_j$), each process in path A is independent of those in path B. For example, in Compton scattering, for fixed θ , conversion to secondaries at the primary-interaction site is independent of conversion at the reabsorption site. As a result, even though \tilde{N}_A and \tilde{N}_B are not normally independent, the PDF of \tilde{N}_A and \tilde{N}_B given $\tilde{N}_0, \tilde{\xi}_A, \tilde{\xi}_B$, and $\{\tilde{\mathbf{b}}_j, j = 1, \dots, \tilde{N}_0\}$ is given by

$$p_{N_{A,B}}(N_A, N_B | \tilde{N}_0, \tilde{\xi}_A, \tilde{\xi}_B, \{\tilde{\mathbf{b}}_j, j = 1, \dots, \tilde{N}_0\}) = p_{N_A}(N_A | \tilde{N}_0, \tilde{\xi}_A, \tilde{\xi}_B, \{\tilde{\mathbf{b}}_j, j = 1, \dots, \tilde{N}_0\}) \times p_{N_B}(N_B | \tilde{N}_0, \tilde{\xi}_A, \tilde{\xi}_B, \{\tilde{\mathbf{b}}_j, j = 1, \dots, \tilde{N}_0\}), \quad (C11)$$

where

$$p_{N_A}(N_A|\tilde{N}_0, \tilde{\xi}_A, \tilde{\xi}_B, \{\tilde{\mathbf{b}}_j, j=1, \dots, \tilde{N}_0\}) \\ = p_{N_{1,A}}(N_A|\tilde{\xi}_{1,A}, \tilde{\mathbf{b}}_1) * \dots * p_{N_{N_0,A}}(N_A|\tilde{\xi}_{N_0,A}, \tilde{\mathbf{b}}_{N_0}). \quad (\text{C12})$$

Combining with the similar p_{N_B} and averaging over all possible values of $\tilde{\xi}_A$, $\tilde{\xi}_B$, and $\{\tilde{\mathbf{b}}_j, j=1, \dots, \tilde{N}_0\}$ yields

$$p_{N_{A,B}}(N_A, N_B|\tilde{N}_0) \\ = \left\langle \left\langle p_{N_A}^{(1)}(N_A|\xi_A, \mathbf{b}) p_{N_{B,1}}(N_B|\xi_B, \mathbf{b}) \right\rangle_{\xi_A, \xi_B} \right\rangle_{\xi_A, \xi_B} \\ *^{N_0-1} \left\langle \left\langle p_{N_A}^{(1)}(N_A|\xi_A, \mathbf{b}) p_{N_{B,1}}(N_B|\xi_B, \mathbf{b}) \right\rangle_{\xi_A, \xi_B} \right\rangle_{\xi_A, \xi_B}, \quad (\text{C13})$$

where $p_{N_A}^{(1)}(N_A|\xi_A, \mathbf{b})$ represents the PDF of \tilde{N}_A given $\xi_{j,A}$ and \mathbf{b}_j for one quantum input to the parallel cascade with a similar result for path B, and

$$\left\langle p_{N_A}^{(1)}(N_A|\xi_A, \mathbf{b}) p_{N_{B,1}}(N_B|\xi_B, \mathbf{b}) \right\rangle_{\mathbf{b}} \\ = \int p_{N_A}^{(1)}(N_A|\xi_A, \mathbf{b}) p_{N_{B,1}}(N_B|\xi_B, \mathbf{b}) p_{\mathbf{b}}(\mathbf{b}) d^m \mathbf{b}, \quad (\text{C14})$$

where $p_{\mathbf{b}}(\mathbf{b}_j) = p_{\mathbf{b}}(\mathbf{b})$ independent of j . Averaging over all possible values of \tilde{N}_0 yields

$$p_{N_{A,B}}(N_A, N_B) = \int \left[\left\langle \left\langle p_{N_A}^{(1)}(N_A|\xi_A, \mathbf{b}) p_{N_{B,1}}(N_B|\xi_B, \mathbf{b}) \right\rangle_{\xi_A, \xi_B} \right\rangle_{\xi_A, \xi_B} \right. \\ *^{N_0-1} \left. \left\langle \left\langle p_{N_A}^{(1)}(N_A|\xi_A, \mathbf{b}) p_{N_{B,1}} \right\rangle_{\xi_A, \xi_B} \right\rangle_{\xi_A, \xi_B} \right] p_{N_0}(N_0) dN_0. \quad (\text{C15})$$

This result is a new contribution and describes the joint PDF of quanta from two parallel paths when parameters of elementary processes in each path are functions of random variables $\tilde{\mathbf{b}}$ associated with each input quantum (depth of interaction and scatter-photon angle in this work).

APPENDIX D: PDF OF REABSORPTION DEPTH \tilde{z}_2

Calculation of the total number of quanta for the generic interaction model [Eq. (62)] requires the PDF of reabsorption depth \tilde{z}_2 given \tilde{z}_1 and $\tilde{\theta}$. Using a cylindrical coordinate system with origin at \tilde{z}_1 , $p_{z_2}(z_2|z_1, \theta)$ is given by

$$p_{z_2}(z_2|\tilde{z}_1, \tilde{\theta}) = \iint p_{z_2}(z_2, r, \phi|\tilde{z}_1, \tilde{\theta}) r dr d\phi, \quad (\text{D1})$$

where $p_{z_2}(z_2, r, \phi|z_1, \theta)$ represents the joint PDF of \tilde{z}_2 , \tilde{r} , and azimuthal angle $\tilde{\phi}$ (Fig. 5) given \tilde{z}_1 and $\tilde{\theta}$,

$$p_{z_2}(z_2, r, \phi|\tilde{z}_1, \tilde{\theta}) = C(\tilde{z}_1, \tilde{\theta}) \mu(E_s) e^{-\mu(E_s) \sqrt{r^2 + (\tilde{z}_1 - z_2)^2}}, \quad (\text{D2})$$

where C is a normalization constant. Assuming the scatter photon is reabsorbed, C is determined by requiring the integral of p_{z_2} over a semi-infinite slab of thickness L to be unity for all \tilde{z}_1 and $\tilde{\theta}$,

$$C(\tilde{z}_1, \tilde{\theta})^{-1} = 2\pi \begin{cases} \int_{\tilde{z}_1}^L \int_{\tilde{z}_1}^{(L-\tilde{z}_1)|\tan\theta} \mu(E_s) e^{-\mu(E_s) \sqrt{r^2 + (\tilde{z}_1 - z_2)^2}} r dr dz_2 & 0 \leq \theta < \pi/2 \\ \int_0^{\tilde{z}_1} \int_{\tilde{z}_1|\tan\theta}^L \mu(E_s) e^{-\mu(E_s) \sqrt{r^2 + (\tilde{z}_1 - z_2)^2}} r dr dz_2 & \pi/2 \leq \theta < \pi \end{cases}. \quad (\text{D3})$$

^{a)} Author to whom correspondence should be addressed. Electronic mail: jessetan@mail.ubc.ca

^{b)} Present address: Department of Radiology, Faculty of Medicine, University of British Columbia, Vancouver, British Columbia V5Z 4E3, Canada.

¹X. Llopart, M. Campbell, D. S. Segundo, E. Pernigotti, and R. Dinapoli, "Medipix2, a 64k pixel read out chip with 55 μm square elements working in single photon counting mode," in *2001 IEEE Nuclear Science Symposium Conference Record* (IEEE, 2001).

²B. Mikulec, "Development of segmented semiconductor arrays for quantum imaging," *Nucl. Instrum. Meth. A* **510**, 1–23 (2003).

³M. Locker, P. Fisher, S. Krimmel, H. Kruger, M. Lindner, K. Nakazawa, T. Takahashi, and N. Wermes, "Single photon counting x-ray imaging with Si and CdTe single chip pixel detectors and multichip pixel modules," *IEEE Trans. Nucl. Sci.* **51**, 1717–1723 (2004).

⁴R. Ballabriga, M. Campbell, E. Heijne, X. Llopart, and L. Tlustos, "The Medipix3 prototype, a pixel readout chip working in single photon counting mode with improved spectrometric performance," *IEEE Trans. Nucl. Sci.* **54**, 1824–1829 (2007).

⁵C. Carpentieri, M. G. Bisogni, A. D. Guerra, P. Delogu, M. E. Fantacci, J. Fogli, A. Marchi, V. Marzulli, V. Rosso, A. Stefanini, and A. Tofani, "A pixel detector-based single photon-counting system as fast spectrometer for diagnostic x-ray beams," *Radiat. Prot. Dosim.* **129**(1–3), 119–122 (2008).

⁶J. S. Iwaczyk, E. Nygard, O. Meirav, J. Arenson, W. C. Barber, N. E. Hartsough, N. Malakhov, and J. C. Wessel, "Photon counting energy dispersive detector arrays for x-ray imaging," *IEEE. Trans. Nucl. Sci.* **56**(3), 535–542 (2009).

⁷K. Taguchi and J. S. Iwaczyk, "Single photon counting x-ray detectors in medical imaging," *Med. Phys.* **40**(10), 100901 (14pp.) (2013).

⁸S. Feuerlein, E. Roessl, R. Proksa, G. Martens, O. Klass, M. Jeltsch, V. Rasche, H.-J. Brambs, M. H. K. Hoffmann, and J.-P. Schlomka, "Multi-energy photon-counting K-edge imaging: Potential for improved luminal depiction in vascular imaging," *Radiology* **249**, 1010–1016 (2008).

⁹X. Liu, L. Yu, A. N. Primak, and C. H. McCollough, "Quantitative imaging of element composition and mass fraction using dual-energy CT: Three-material decomposition," *Med. Phys.* **36**, 1602–1609 (2009).

¹⁰P. M. Shikhaliev, "Projection x-ray imaging with photon energy weighting: Experimental evaluation with a prototype detector," *Phys. Med. Biol.* **54**, 4971–4992 (2009).

¹¹E. Fredenberg, M. Hemmendorff, B. Cederstrom, M. Aslund, and M. Danielsson, "Contrast-enhanced spectral mammography with a photon-counting detector," *Med. Phys.* **37**, 2017–2029 (2010).

¹²M. A. Hurrell, A. P. H. Butler, N. J. Cook, P. H. Butler, J. P. Ronaldson, and R. Zainon, "Spectral hounsfield units: A new radiological concept," *Eur. Radiol.* 1008–1013 (2011).

¹³J. Tanguay, H. K. Kim, and I. A. Cunningham, "A theoretical comparison of x-ray angiographic image quality using energy-dependent and conventional subtraction methods," *Med. Phys.* **39**, 132–142 (2012).

¹⁴P. Baturin, Y. Alivov, and S. Molloy, "Spectral ct imaging of vulnerable plaque with two independent biomarkers," *Phys. Med. Biol.* **57**, 4117–4138 (2012).

¹⁵M. J. Tapiovaara and R. F. Wagner, "SNR and DQE analysis of broad spectrum x-ray imaging," *Phys. Med. Biol.* **30**, 519–529 (1985).

- ¹⁶M. Lundqvist, B. Cederstrom, V. Chmill, M. Danielsson, and B. Hasegawa, "Evaluation of a photon counting x-ray imaging system," in *2000 IEEE Nuclear Science Symposium Conference Record* (IEEE, 2000), Vol. 1, pp. 3–6.
- ¹⁷L. Abbene, G. Gerardi, F. Principato, S. Del Sordo, R. Ienzi, and G. Raso, "High-rate x-ray spectroscopy in mammography with a CdTe detector: A digital pulse processing approach," *Med. Phys.* **37**(12), 6147–6156 (2010).
- ¹⁸F. F. Schmitzberger, E. M. Fallenberg, R. Lawaczeck, M. Hemmendorff, E. Moa, M. Danielsson, U. Bick, S. Diekmann, A. Pollinger, F. J. Engelken, and F. Diekmann, "Development of low-dose photon-counting contrast-enhanced tomosynthesis with spectral imaging," *Radiology* **259**, 558–564 (2011).
- ¹⁹L. Abbene, G. Gerardi, F. Principato, S. Del Sordo, and G. Raso, "Direct measurement of mammographic x-ray spectra with a digital CdTe detection system," *Sensors (Basel)* **12**(6), 8390–8404 (2012).
- ²⁰E. Fredenberg, D. R. Dance, P. Willsher, E. Moa, M. von Tiedemann, K. C. Young, and M. G. Wallis, "Measurement of breast-tissue x-ray attenuation by spectral mammography: First results on cyst fluid," *Phys. Med. Biol.* **58**, 8609–8620 (2013).
- ²¹P. M. Shikhaliev, "Energy-resolved computed tomography: First experimental results," *Phys. Med. Biol.* **53**, 5595–5613 (2008).
- ²²P. M. Shikhaliev and S. G. Fritz, "Photon counting spectral CT versus conventional CT: Comparative evaluation for breast imaging application," *Phys. Med. Biol.* **56**, 1905–1930 (2011).
- ²³H. Ding, M. J. Klopfer, J. L. Ducote, F. Masaki, and S. Molloy, "Breast tissue characterization with photon-counting spectral ct imaging: A postmortem breast study," *Radiology*, **272**(3), 731–738 (2014).
- ²⁴S. Weigel, S. Berkemeyer, R. Girnus, A. Sommer, H. Lenzen, and W. Heindel, "Digital mammography screening with photon-counting technique: Can a high diagnostic performance be realized at low mean glandular dose?," *Radiology* **271**, 345–355 (2014).
- ²⁵M. Yveborg, M. Danielsson, and H. Bornefalk, "Performance evaluation of a sub-millimetre spectrally resolved ct system on high- and low-frequency imaging tasks: A simulation," *Phys. Med. Biol.* **57**, 2373–2391 (2012).
- ²⁶A. M. Alessio and L. R. MacDonald, "Quantitative material characterization from multi-energy photon counting CT," *Med. Phys.* **40**, 031108 (8pp.) (2013).
- ²⁷H. Bornefalk, C. Xu, C. Svensson, and M. Danielsson, "Design considerations to overcome cross talk in a photon counting silicon strip detector for computed tomography," *Nucl. Instrum. Meth. A* **621**, 371–378 (2010).
- ²⁸X. Wang, D. Meier, S. Mikkelsen, G. E. Maehlum, D. J. Wagenaar, B. M. W. Tsui, B. E. Patt, and E. C. Frey, "MicroCT with energy-resolved photon-counting detectors," *Phys. Med. Biol.* **56**, 2791–2816 (2011).
- ²⁹A. Korn, M. Firsching, G. Anton, M. Hoheisel, and T. Michel, "Investigation of charge carrier transport and charge sharing in x-ray semiconductor pixel detectors such as Medipix2," *Nucl. Instrum. Meth. A* **576**, 239–242 (2007).
- ³⁰P. M. Shikhaliev, S. G. Fritz, and J. W. Chapman, "Photon counting multi-energy x-ray imaging: Effect of the characteristic x rays on detector performance," *Med. Phys.* **36**, 5107–5119 (2009).
- ³¹R. J. Acciavatti and D. A. Maidment, "A comparative analysis of OTF, NPS, and DQE in energy integrating and photon counting digital x-ray detectors," *Med. Phys.* **37**, 6480–6495 (2010).
- ³²M. Rabbani, R. Shaw, and R. V. Metter, "Detective quantum efficiency of imaging systems with amplifying and scattering mechanisms," *J. Opt. Soc. Am. A* **4**, 895–901 (1987).
- ³³I. A. Cunningham, M. S. Westmore, and A. Fenster, "A spatial-frequency dependent quantum accounting diagram and detective quantum efficiency model of signal and noise propagation in cascaded imaging systems," *Med. Phys.* **21**, 417–427 (1994).
- ³⁴J. H. Siewerdsen, L. E. Antonuk, Y. el Mohri, J. Yorkston, W. Huang, J. M. Boudry, and I. A. Cunningham, "Empirical and theoretical investigation of the noise performance of indirect detection, active matrix flat-panel imagers (AMFPIs) for diagnostic radiology," *Med. Phys.* **24**, 71–89 (1997).
- ³⁵I. A. Cunningham and R. Shaw, "Signal-to-noise optimization of medical imaging systems," *J. Opt. Soc. Am. A* **16**, 621–632 (1999).
- ³⁶I. A. Cunningham, *Handbook of Medical Imaging* (SPIE, Bellingham, WA, 2000), Chap. 2, pp. 79–160.
- ³⁷S. Richard, J. H. Siewerdsen, D. A. Jaffray, D. J. Moseley, and B. Bakhtiar, "Generalized DQE analysis of radiographic and dual-energy imaging using flat-panel detectors," *Med. Phys.* **32**, 1397–1413 (2005).
- ³⁸G. Hajdok, J. Yao, J. J. Battista, and I. A. Cunningham, "Signal and noise transfer properties of photoelectric interactions in diagnostic x-ray imaging detectors," *Med. Phys.* **33**, 3601–3620 (2006).
- ³⁹R. Akbarpour, S. N. Friedman, J. H. Siewerdsen, J. D. Neary, and I. A. Cunningham, "Signal and noise transfer in spatiotemporal quantum-based imaging systems," *J. Opt. Soc. Am. A Opt. Image Sci. Vis.* **24**, B151–B164 (2007).
- ⁴⁰G. Hajdok, J. J. Battista, and I. A. Cunningham, "Fundamental x-ray interaction limits in diagnostic imaging detectors: Frequency-dependent Swank noise," *Med. Phys.* **35**, 3194–3204 (2008).
- ⁴¹S. Yun, J. Tanguay, H. K. Kim, and I. A. Cunningham, "Cascaded-systems analysis and the detective quantum efficiency of single-Z x-ray detectors include photoelectric, coherent and incoherent interactions," *Med. Phys.* **40**, 041916 (16pp.) (2013).
- ⁴²J. Tanguay, S. Yun, H. K. Kim, and I. A. Cunningham, "Cascaded systems analyses of photon-counting x-ray detectors," *Proc. SPIE* **8668**, 0S1–0S14 (2013).
- ⁴³J. Tanguay, S. Yun, H. K. Kim, and I. A. Cunningham, "The detective quantum efficiency of photon-counting x-ray detectors using cascaded systems analyses," *Med. Phys.* **40**, 041913 (15pp.) (2013).
- ⁴⁴R. K. Swank, "Absorption and noise in x-ray phosphors," *J. Appl. Phys.* **44**, 4199–4203 (1973).
- ⁴⁵R. K. Swank, "Measurement of absorption and noise in an x-ray image intensifier," *J. Appl. Phys.* **45**, 3673–3678 (1974).
- ⁴⁶J. Tanguay, H. K. Kim, and I. A. Cunningham, "The role of x-ray swank factor in energy-resolving photon-counting imaging," *Med. Phys.* **37**, 6205–6211 (2010).
- ⁴⁷S. Yun, H. K. Kim, H. Youn, J. Tanguay, and I. A. Cunningham, "Analytic model of energy-absorption response functions in compound x-ray detector materials," *IEEE Trans. Med. Imaging* **32**, 1819–1828 (2013).
- ⁴⁸K. Taguchi, E. C. Frey, X. Wang, J. S. Iwanczyk, and W. C. Barber, "An analytical model of the effects of pulse pileup on the energy spectrum recorded by energy resolved photon counting x-ray detectors," *Med. Phys.* **37**, 3957–3969 (2010).
- ⁴⁹A. S. Wang, D. Harrison, V. Lobastov, and J. E. Tkaczyk, "Pulse pileup statistics for energy discriminating photon counting x-ray detectors," *Med. Phys.* **38**, 4265–4275 (2011).
- ⁵⁰E. Roessl, H. Daerra, K. J. Engel, A. Thran, C. Schirra, and R. Proksa, "Combined effects of pulse pile-up and energy response in energy-resolved, photon-counting computed tomography," in *IEEE Nuclear Science Symposium Conference Record* (IEEE, 2011), pp. 2309–2313.
- ⁵¹R. Bracewell, *The Fourier Transform and its Applications*, 3rd ed. (McGraw-Hill Science, New York, NY, 1999).
- ⁵²S. N. Friedman and I. A. Cunningham, "A spatio-temporal detective quantum efficiency and its application to fluoroscopic systems," *Med. Phys.* **37**(11), 6061–6069 (2010).
- ⁵³J. Yao and I. A. Cunningham, "Parallel cascades: New ways to describe noise transfer in medical imaging systems," *Med. Phys.* **28**, 2020–2038 (2001).
- ⁵⁴M. Sattarivand and I. A. Cunningham, "Computational engine for development of complex cascaded models of signal and noise in x-ray imaging systems," *IEEE Trans. Med. Imaging* **24**(2), 211–222 (2005).
- ⁵⁵A. Papoulis, *Probability, Random Variables, and Stochastic Processes*, 3 ed. (McGraw-Hill, Inc., New York, NY, 1991).
- ⁵⁶R. V. Metter and M. Rabbani, "An application of multivariate moment-generating functions to the analysis of signal and noise propagation in radiographic screen-film systems," *Med. Phys.* **17**(1), 65–71 (1990).
- ⁵⁷W. Shockley, "Currents to conductors induced by a moving point charge," *J. Appl. Phys.* **9**(10), 635–636 (1938).
- ⁵⁸S. Ramo, "Currents induced by electron motion," *Proc. IRE* **27**(9), 584–585 (1939).
- ⁵⁹K. Hecht, "Zum mechanismus des lichtelektrischen primarstromes in isolierenden kristallen," *Z. Phys.* **77**, 235–245 (1932).
- ⁶⁰G. Knoll, *Radiation Detection and Measurement* (Wiley, New York, NY, 2000).
- ⁶¹S. O. Kasap, "X-ray sensitivity of photoconductors: Applications to stabilized a-Se," *J. Phys. D: Appl. Phys.* **33**, 2853–2865 (2000).
- ⁶²J. Tanguay, H. K. Kim, and I. A. Cunningham, "Extension of cascaded systems analysis to single-photon-counting x-ray detectors," *Proc. SPIE* **8313**(10), 1–13 (2012).
- ⁶³G. Hajdok, J. J. Battista, and I. A. Cunningham, "Fundamental x-ray interaction limits in diagnostic imaging detectors: Spatial resolution," *Med. Phys.* **35**, 3180–3193 (2008).
- ⁶⁴F. H. Attix, *Introduction to Radiological Physics and Radiation Dosimetry* (Wiley-Interscience, New York, NY, 1986).

- ⁶⁵T. R. Melzer, N. J. Cook, A. P. Butler, R. Watts, N. Anderson, R. Tipples, and P. H. Butler, "Spectroscopic biomedical imaging with the Medipix2 detector," *Australas. Phys. Eng. Sci. Med.* **31**, 300–306 (2008).
- ⁶⁶R. van Gastel, I. Sikharulidze, S. Schramm, J. P. Abrahams, B. Poelsema, R. M. Tromp, and S. J. van der Molen, "Medipix 2 detector applied to low energy electron microscopy," *Ultramicroscopy* **110**, 33–35 (2009).
- ⁶⁷J. A. Rowlands and J. Yorkston, *Handbook of Medical Imaging* (SPIE, Bellingham, WA, 2000), Chap. 4, pp. 223–329.
- ⁶⁸C. Xu, M. Danielsson, and H. Bornefalk, "Evaluation of energy loss and charge sharing in cadmium telluride detectors for photon-counting computed tomography," *IEEE Trans. Nucl. Sci.* **58**, 614–625 (2011).